Distribution Agreement

In presenting this thesis or dissertation as a partial fulfillment of the requirements for an advanced degree from Emory University, I hereby grant to Emory University and its agents the non-exclusive license to archive, make accessible, and display my thesis or dissertation in whole or in part in all forms of media, now or hereafter known, including display on the world wide web. I understand that I may select some access restrictions as part of the online submission of this thesis or dissertation. I retain all ownership rights to the copyright of the thesis or dissertation. I also retain the right to use in future works (such as articles or books) all or part of this thesis or dissertation.

Signature:

Skanda Vivek	Date

The role of dimension and shape in colloidal liquids and glasses

by
Skanda Vivek
Doctor of Philosophy
Physics

Eric Richard Weeks, Ph.D
Advisor

Connie Roth, Ph.D
Committee Member

Jennifer Curtis, Ph.D
Committee Member

Minsu Kim, Ph.D
Committee Member

Stefan Boettcher, Ph.D
Committee Member

Accepted:

Lisa A. Tedesco, Ph.D.
Dean of the James T. Laney School of Graduate Studies

Date

The role of dimension and shape in colloidal liquids and glasses

by

Skanda Vivek
M.Sc., Indian Institue of Technology, Bombay 2011
B.Sc., St. Josephs College, Bangalore 2009

Advisor: Eric R. Weeks, Ph.D.

An abstract of
A dissertation submitted to the Faculty of the
James T. Laney School of Graduate Studies of Emory University
in partial fulfillment of the requirements for the degree of
Doctor of Philosophy
in Physics
2016

Abstract

The role of dimension and shape in colloidal liquids and glasses

By Skanda Vivek

In two-dimensions, the laws of physics give rise to intriguing phenomena such as long-range correlations that do not decay at infinity. However, reality can only be quasi-2D at best. This thesis is an effort to bridge the gap between 2D theory and reality, by doing experiments. Here we consider two different model systems - soap films as 2D fluids, and 2D colloidal glass formers.

We look at diffusion of tracer particles in soap films and test the validity of 2D theory. We find that for thin films, both 2D surface viscosity and 3D viscosity are important. To a good approximation, soap films are thin films and can be considered 2D for flow.

Next, we look at glassy dynamics in 2D and 3D colloidal glass formers. We demonstrate that the differences between 2D and 3D are long-wavelength fluctuations, precisely those that distinguish 2D and 3D phase transitions. Through a novel analysis method that removes the influence of these fluctuations, we show that 2D and 3D glass transitions are otherwise similar.

Finally, we look at the effect of shape anisotropy of dimers in 2D glasses, and find that glass dynamics are highly dependent on shape, both in experiments and simulations. These colloidal and simulation results are a prediction of aspect ratio dependent diffusion in real glasses.

The role of dimension and shape in colloidal liquids and glasses

by

Skanda Vivek
M.Sc., Indian Institute of Technology,Bombay 2011
B.S., St. Josephs College, Bangalore, 2009

Advisor: Eric R. Weeks, Ph.D.

A dissertation submitted to the Faculty of the
James T. Laney School of Graduate Studies of Emory University
in partial fulfillment of the requirements for the degree of
Doctor of Philosophy
in Physics
2016

Acknowledgements

I thank my advisor Eric R. Weeks for his awesome mentorship. Thanks to Eric's mentoring, I feel a vast improvement in my research, approaching problems and being more collaborative. I always got great feedback from Eric and he was very supportive of my ideas and side endeavors. I also thank my committee members, Stefan Boettcher, Jennifer Curtis, Minsu Kim, and Connie Roth for serving as my committee and their valuable advice.

My time at the Weeks lab was great, I had very helpful inputs on research and great fun outside the lab. In particular I thank Carlos Orellana, Cao Cong, Thibaut Divoux, Ken Desmond, Xin Du and Xia Hong. I thank my collaborators Colm Kelleher and Paul Chaikin at NYU. I thank my other collaborators at Emory: Kevin Yehl, Kevin Sullivan, Huiling Jiang, Stefan Boettcher, Khalid Salaita, Craig Hill and Yonggang Ke. I thank Josh Savory for help with the lock-in amplifier. Thanks for the wonderful work and for reminding me that science does not happen in a bubble.

I thank the Young Emory Physicists (YEP) organization and especially Benjamen Nforneh, George Leung, Ryan Freeman, Xinru, Huang, Baohua Zhou, Vijay Singh, Guga Gogia, Andrei Zholud, Catalina Rivera and Xiang Cheng. At Emory I am part of an awesome community, which was crucial for me during my PhD. I also thank Daniel Garcia and Layla Pournajaf. I am very appreciative of the support staff and specially Jason Boss, Calvin Jackson, Art Kleyman and Barbara Conner.

I thank my girlfriend Chao Song for her invaluable support over the years. Thanks for enduring the moments of craziness and always being loving. Most importantly, I thank my parents, grandparents, and my uncle and aunt. Without you as my role models and encouraging me to pursue my passion, I would not be here. Finally, I thank Emory and

the Laney graduate school for the wonderful support. Financial support for this research was provided by the National Science Foundation Grants CMMI-1250235 and CBET-0853837.

Table of Contents

List of Figures

Citations to Previously Published Work

Chapter 2 contains research from one publication:

1. Skanda Vivek, Eric R. Weeks, Measuring and Overcoming Limits of the Saffman-Delbrück Model for Soap Film Viscosities, *Plos One*, 10, e0121981 (2015)

Chapter 3 contains research from one publication:

2. Skanda Vivek, Colm P. Kelleher, Paul M. Chaikin, Eric R. Weeks, Long Wavelength Fluctuations and the Glass Transition in 2D and 3D, To be published in *Proc. Natl. Acad. Sci.* , arXiv:1604.07338v2 (2016)

Chapter 4 manuscript under preparation:

3. Skanda Vivek, Eric R. Weeks, To be submitted to *J. Chem. Phys.*

Chapter 1

Introduction

1.1 Dimensionality and physics

Many times when we talk about physical phenomena, we ignore dimensionality. For example in introductory physics when dealing with the laws of motion, we first discuss one-dimensional motion, and generalize to two and then three-dimensions. However dimensionality affects physics in many problems such as electrostatics, melting of solids and fluid flows.

The underlying reason is that in 2D, logarithmic decays appear frequently. The electric potential from a line charge of infinite length decays as $\ln(r)$. Flow velocities in a 2D fluid also decay logarithmically, leading to the 'Stokes paradox,' where the standard Navier-Stokes equations in the laminar regime (Stokes regime) do not have non zero solutions for unbounded systems. Even in 2D solids, perturbations decay logarithmically, leading to 'Mermin-Wagner fluctuations' [1] that break true long-range order in 2D solids.

However, reality can only be quasi-2D. According to famous fluid dynamicist George Keith Batchelor (GKB) in an exchange that took place during a seminar in Cambridge

in the mid 1970s [2]:

Speaker (justifying elaborate mathematical argument): The trouble with a physical argument is that you may not get all the terms.

GKB: No, that is the trouble with a bad physical argument.

It is important to understand the validity of 2D theory and approximations in reality where systems are bounded and interfaces matter. This has become very important lately due to recent technical developments in synthesizing 2D materials such as graphene [3] with unique properties.

During my PhD, I have looked at the influence of dimensionality in different materials. Through this thesis, I will demonstrate that in certain cases, dimensionality changes physics, but in others, dimensionality effects can be disentangled from the underlying physics.

I look at two experimental model systems of low-dimensional liquids and amorphous solids (glasses). I do experiments in thin soap films and test the validity of 2D theory. I find that for thin films, both 2D surface viscosity and 3D viscosity are important. To a good approximation, soap films are thin films and can be considered 2D for flow.

For 2D glasses, there is no complete theory for glasses in general, however I find that dimensionality can be separated out, and that being in 2D does not affect underlying glassy physics. This represents a fundamentally different way of disentangling the influence of dimensionality, and may pave the way for future studies in dimensionality in other types of systems. Also I look at the effect of particle shape in 2D glasses, and find that glass dynamics are highly dependent on shape, both in experiments and simulations.

1.2 Liquids and dimensionality

The Navier-Stokes equation for a Newtonian viscous fluid of constant density and constant viscosity is

$$\rho\frac{\partial \mathbf{u}}{\partial t} + \rho\mathbf{u}\cdot\nabla\mathbf{u} - \eta\nabla^2\mathbf{u} = -\nabla p \tag{1.1}$$

where $\mathbf{u}$ is the flow velocity, P is the pressure, and η is the viscosity. In the Stokes regime, viscous forces are much more important than inertial forces. The Reynolds number Re=inertial forces/viscous forces $= \rho UL/\eta \ll 1$, where ρ is density, U is velocity of object relative to fluid and L is the lengthscale of the object. In the Stokes regime since inertia and hence terms containing ρ/η are unimportant, the Navier-Stokes equation simplifies to

$$\nabla p - \eta\nabla^2\mathbf{u} = 0 \tag{1.2}$$

This equation in conjunction with the continuity equation for an incompressible fluid ($\nabla\cdot\mathbf{u} = 0$) are known as the Stokes equations. This major simplification is useful when viscosities are large, or flow length-scales are very small. The flow scales in my liquid experiments are in the Stokes regime. In 3D, the Stokes equations can be solved in the case of a sphere in an infinite fluid. However in 2D, there is not satisfactory steady solution of the Stokes equations representing flow of an unbounded fluid past a circular cylinder. This result, known as Stokes paradox [4], underlines the profound effect that dimension can play in fluid dynamics. The reason for this is a cylindrical body in creeping through a viscous fluid will tend to carry with it a large stagnant body of fluid, and there is no solution of the boundary-value problem for an infinite domain in Stokes flow.

It is convenient and useful to approximate external forces from spheres in 3D as point

forces of magnitude F,

$$\nabla p - \eta \nabla^2 \mathbf{u} = \mathbf{F}\delta(r) \tag{1.3}$$

The solution to this equation in 3D is [5]:

$$u_i = \frac{1}{8\pi\mu r}\left[\frac{r_i r_j}{r^2} + \delta_{ij}\right] F_j \tag{1.4}$$

where r denotes distance from point disturbance. Thus, at large r, flow velocity decays to zero, which is reasonable. However in quasi-2D for thin films of thickness h, the solution is [5, 6]:

$$u_i = \frac{1}{4\pi\mu h}\left[\frac{r_i r_j}{r^2} + \delta_{ij}\left(-\ln r - 1\right)\right] F_j \tag{1.5}$$

This solution is not bounded at infinity, and does not represent real fluids, where other effects are important over large distances. In a recent approximation, Di Leonardo *et al* [6] added an integration constant L, beyond which the approximation fails as:

$$u_i = \frac{1}{4\pi\mu h}\left[\frac{r_i r_j}{r^2} + \delta_{ij}\left(\ln\frac{L}{r} - 1\right)\right] F_j \tag{1.6}$$

This L can have various origins - finite boundaries, particle velocity relative to fluid[2, 6, 7], surrounding fluid etc. Di Leonardo *et al* [6] used colloidal particles as tracers in thin liquid films, and measured hydrodynamic interactions between colloidal particles confined in a thin sheet of fluid. In their experiments, boundary conditions determined L. L was found to be 2 mm, while particle diameter was 2μm. Thus in 2D, correlation length scales are huge as compared to 3D. To give an idea, previous experiments in 3D [8] observed two-point correlations between colloidal particles decay as $1/r$, as expected in

theory, so for a factor of 10 increase in distance, two-point correlations decay by 0.1. Whereas in 2D, two-point correlations decay as $\ln(r)$. Thus these correlations are still large even at large distances in 2D.

1.3 2D viscosity

Viscosity is a measure of a fluids resistance to shear. For a shear force F acting on area A,

$$F = \eta A \frac{\partial u}{\partial y} \tag{1.7}$$

where $\partial u/\partial y$ denotes the shear strain and η is the viscosity. Thus shear stress $\tau = F/A$ is proportional to shear strain rate, and the constant of proportionality is viscosity η. The units of viscosity are Pa·s

In 2D, however, the situation is different. Because of dimensionality, it is not possible to have shear stresses, instead you have line stresses and F/A is replaced by F/l as proportional to shear strain rate. Thus 2D viscosity η_{2D} is fundamentally different from 3D, and has units of Pa·s·m.

For a sphere diffusing in a fluid, the Navier-Stokes equation in the Stokes limit (Eqn. 1.2) can be solved to get the diffusion coefficient,

$$D = \frac{k_B T}{3\pi \eta_{3D} d}, \tag{1.8}$$

known as the Stokes-Einstein-Sutherland equation [9, 10] where η_{3D} is the viscosity of surrounding fluid. However in 2D, the equation cannot be solved in the exact same limit due to the Stokes paradox (Sec. 1.2).

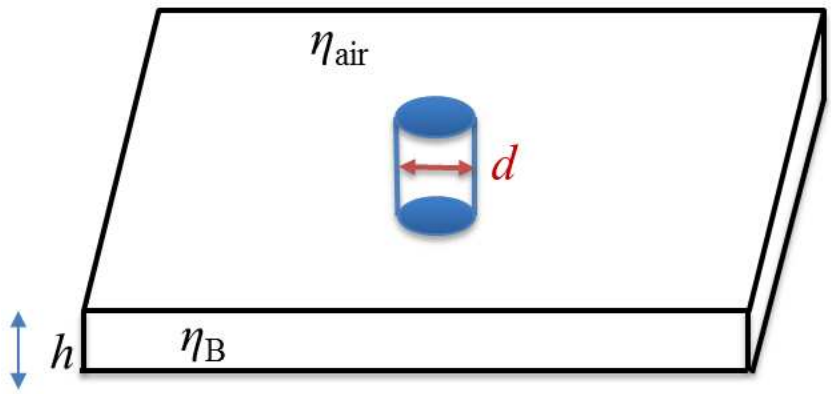

Figure 1.1: Cylinder of diameter d diffusing in a thin film of thickness h and viscosity η_B bounded by air. Model system for deriving 2D Saffman and Delbrück equations.

In 1975 Saffman and Delbrück treated this case, deriving an approximation for single particle diffusion D_{1p}, for the situation of a 2D membrane with interfacial viscosity η_{2D} with fluid of 3D viscosity η_{3D} on both sides of the membrane [11]. Using the small parameter $\epsilon = d\eta_{3D}/\eta_{2D}$, Saffman and Delbrück found [11, 12]

$$D_{1p} = \frac{k_B T}{4\pi\eta_{2D}} \left[\ln\left(\frac{2}{\epsilon}\right) - \gamma_E \right], \tag{1.9}$$

using Euler's constant $\gamma_E = 0.577$.

In particular, this derivation treated the 2D membrane as a thin 3D layer of fluid with 3D ("bulk") viscosity η_B, thickness h, and therefore a 2D viscosity $\eta_{2D} = h\eta_B$. They considered the diffusion of disks of diameter d and height h which spanned the membrane thickness, and which only move horizontally within the membrane (see Fig. 1.1). Equation 1.9 works well for small ϵ (large η_{2D}). ϵ^{-1} is often termed the Boussinesq number Bo, so equivalently Eqn. 1.9 works well for large Bo. [2, 13]. Hughes *et al.* [14] extended Eqn. 1.9 to work for all ϵ, with a useful approximation to their result added later by others [15, 16].

There have been many experiments to verify the Saffman-Delbruck equation and its large ϵ extensions, such as in in lipid membranes [16] and liquid crystal films [17].

In our experiments, we use thin soap films as model 2D fluids (Chapter 2) embedded with spherical tracers, and rather than checking the validity of these equations in the ϵ limit, we look at the 2D-3D transition as a function of soap film thickness h and tracer particle diameter d. All our experiments are in the low ϵ limit. Interestingly we find that h/d is the control parameter, and for small h/d, single particle diffusion follows 2D theory as per Eqn. 1.9. But for large h/d particles tend towards bulk diffusion as in Eqn. 1.8.

1.4 Solids and dimensionality

The influence of dimensionality in solids has been studied as early as in the 1930's by Peierls [18]. An elegant argument put forward for one-dimensional solids is that any random fluctuations get amplified in 1D, thus long-range order is not possible in 1D.

Figure 1.2 shows a 1D solid with periodicity a. Due to thermal fluctuations, there is a fluctuation σ. Assuming these fluctuations are statistically independent, the total standard deviation Sigma adds up as $\sqrt{N}\sigma$. Thus at long distances for large N, order is destroyed. Hence it is not possible to have a 1D crystal.

In 2D the situation is different. There are more constraints as on a square periodic lattice for example and atoms on the lattice have more neighbors than in 1D. Now, fluctuations need to be correlated along along multiple paths in order to add up, hence fluctuations grows as $\ln N$. Thus fluctuations do not grow as much as in 1D, and it is still possible to have quasi-long-range order in 2D. These fluctuations at very large N are called Mermin-Wagner fluctuations [19]. Their effect in real systems was unclear. To quote Mermin [1], these fluctuations "may well be so weak as to allow two-dimensional

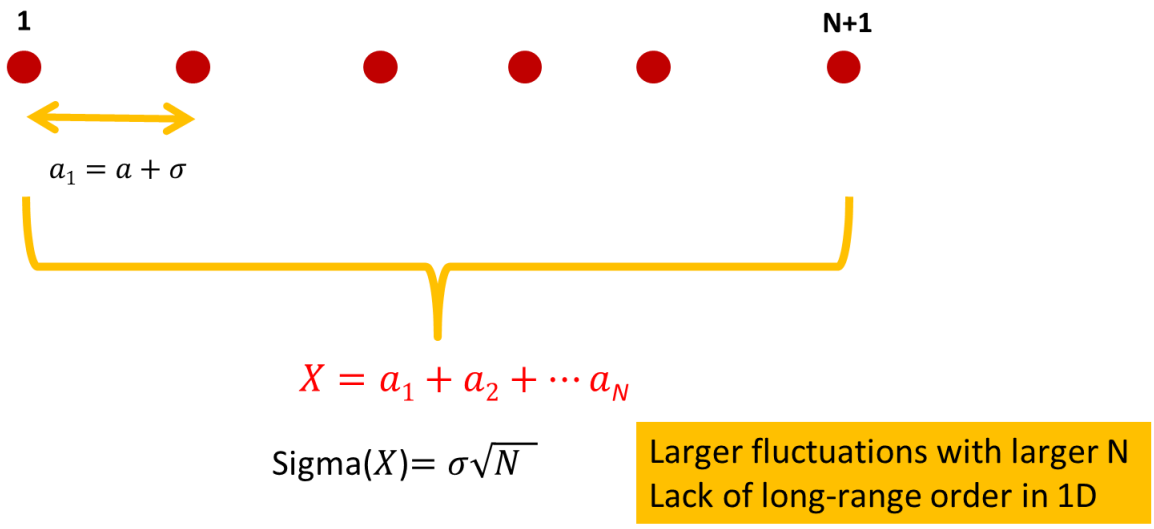

Figure 1.2: 1D solid of lattice spacing a represented by a linear chain of $N+1$ atoms. σ denotes standard deviation due to thermal fluctuations. Assuming these fluctuations add independently, The distance X between the first and the last atom has standard deviation Sigma(X)=$\sigma\sqrt{N}$.

systems of less than astronomic size to display crystalline order." In 3D, fluctuations have to be correlated along even more paths than 2D to add up, so instead fluctuations decay with N, thus preserving true long-range order.

The impact of these fluctuations is profound in 2D [20]. Because of absence of true long-range order, during melting one encounters a solid $\rightarrow$ hexatic $\rightarrow$ liquid transition, as theorized by the KTHNY theory of 2D melting [21] developed by John Kosterlitz, David Thouless, Burt Halperin, David Nelson, and Peter Young. This hexatic phase denotes quasi-long-range bond-orientational order, but short-range translational order [21]. This phase is absent in 3D. Hence dimensionality causes fundamental differences in 2D and 3D melting. Recent experiments [22] and simulations [23] have confirmed that 2D melting indeed involves two steps and follows the KTHNY theory.

1.5 The glass transition and the colloidal glass transition

If a liquid can be cooled rapidly to avoid crystallization, it can form into a glass: an amorphous solid. The transition from liquid to glass on decreasing temperature is a dynamic transition.

The glass transition is marked by an increase in viscosity on decreasing temperature, by more than 13 orders of magnitude. Typically the glass transition temperature T_g is defined when viscosities reach such large values$\sim 10^{12}$ times the viscosity of water [24] when for all practical purposes, the sample is a solid and does not flow on any reasonable experimental timescale. However from a theoretical standpoint, the underlying cause of the glass transition is far from clear, although there are a variety of theories [25–27].

Colloidal samples at high concentration have been established as model glass formers [28–31]. Colloidal experiments have the advantage that individual particles can be visualized. The way the colloidal glass transition is approached is by increasing concentration. Thus concentration in colloidal systems is equivalent to inverse temperature in real glasses. At a low concentration, colloids diffuse in liquids according to the Stokes-Einstein-Sutherland equation (Eqn. 1.8).

Figure 1.3a shows silica particles diffusing in water, confined to a coverslip. On increasing concentration in a bidisperse sample, we get a supercooled liquid shown in Fig. 1.3b. At even higher concentrations, we get a colloidal glass shown in Fig. 1.3c. The difference between supercooled liquid and glass is that the glassy sample does not equilibrate on the experimental timescale.

In 3D colloidal glasses, the situation is well established. The experimental glass transition is at volume fraction $\phi \sim 0.58$ [29].

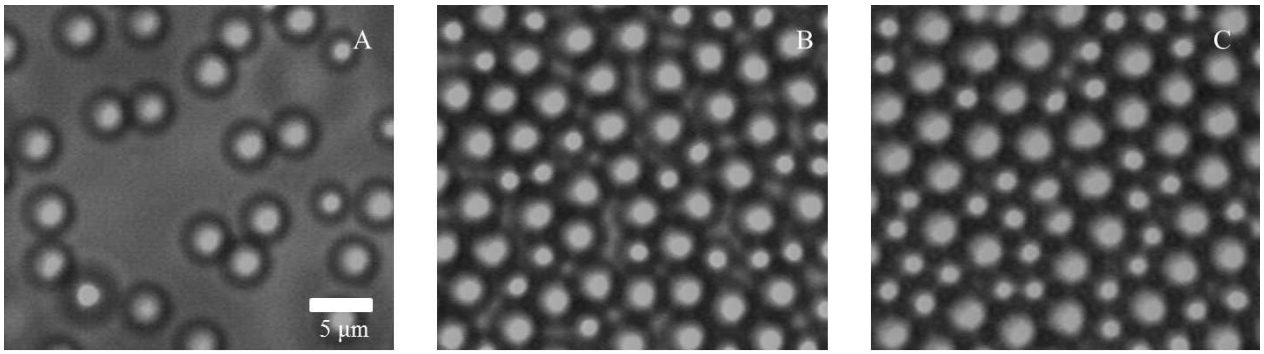

Figure 1.3: Colloidal liquid and solid of bidisperse particles, diameter 2.53 and 3.38 μm. (A) Area fraction $\phi = 0.16$, liquid-like. (B) Area fraction $\phi = 0.70$, supercooled sample. (C) Area fraction $\phi = 0.82$, glassy sample.

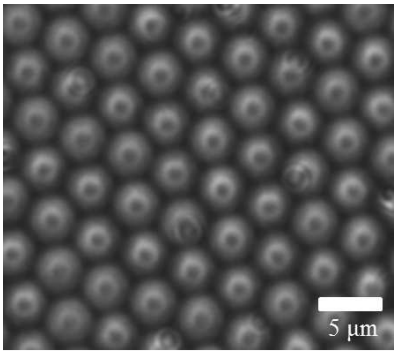

Figure 1.4: Colloidal crystal at $\phi = 0.91$ composed of monodisperse particles of diameter 3.38 μm.

A polydisperse (here bidisperse) sample is needed, which is especially important in 2D, to frustrate formation of local crystals. If the system is monodisperse, we get a colloidal crystal at large $\phi \sim 0.9$ as shown in Fig. 1.4. However in 3D, natural polydispersity from experimental preparation of particles is sufficient to form colloidal glasses.

While the glass transition is itself far from clear, it is usually thought to be similar in 2D and 3D [30, 32] and in simple simulation cases such as hard particles, one might expect that dimensionality plays no role. However, recent simulations give evidence that the glass transition might be quite different in 2D and 3D [33–35]. Comparing 2D and

3D colloidal experiments, I find that it is possible to separate out dimensionality effects from the underlying glassy physics, which is explained in detail in Chapter 3.

1.6 The shape dependent glass transition

The above colloidal glass transition discussed were hard sphere model systems. A lot of molecular and polymer glasses however, do not have radially isotropic molecules. Polymer glasses [24] have long entangled chains, and molecular glasses such as glycerol and OTP [24] have anisotropic shapes.

However, colloidal glasses and simulations of spheres or disks with polydispersity have been very successful in modeling the key features universal to all glass formers. This means that geometrical frustration and sterical confinement in model glasses are key to the glass transition in general.

Due to recent advances in synthesis of anisotropic colloids [36–38] and simulation of anisotropic probes [39, 40], now it is possible to ask the question how does shape anisotropy affect the glass transition. In my experiments (Chapter 4), I study how diffusion properties are affected by shape in a model 2D colloidal glass former. The two modes of diffusion are translation, and rotation associated with rotational motion of anisotropic particles that can be measured.

In liquids, the Stokes-Einstein-Sutherland equation [9, 10] relates microscopic translational diffusion (D_T) as inversely proportional to solvent viscosity η, shown in Eqn. 1.8, where a is particle radius and T is temperature.

For spherical particles, rotational diffusion follows Eqn. 1.10. This is known as the

Stokes-Einstein-Debye relation and was originally found by Debye [41].

$$D_R = \frac{k_B T}{8\pi\eta a^3}, \tag{1.10}$$

In simple liquids, both viscosity and diffusion are linked to a single timescale of structural relaxation. Further, the ratio of translational to rotational diffusion constants (D_T/D_R) should be independent of viscosity and temperature. However, many experiments and simulations [42–45] have shown a violation of the Stokes-Einstein-Sutherland and Stokes-Einstein-Debye relations in supercooled liquids. Pioneering experiments observed a violation of these relations on approaching the glass transition in a molecular glass former, orthoterphenyl (OTP) [42, 43]. The traditional method to determine diffusion coefficients is through mean square displacements:

$$\langle \Delta r^2(\Delta t) \rangle = 4 D_T \Delta t \tag{1.11}$$

Rotational diffusion coefficient (D_R) is measured from mean rotational MSD as:

$$\langle \Delta\theta^2(\Delta t) \rangle = 2 D_R \Delta t \tag{1.12}$$

where $\Delta\theta$ is the angular displacement in time Δt. However in OTP, only indirect measurements of diffusion was possible, from spin-spin relaxations. They found that $D_{T,R} \sim \eta^{-\xi}$, where $\xi = 0.75$ for translation, and 1 for rotation. Thus they observed an enhancement of translation relative to rotation approaching the glass transition. Later experiments in molecular glasses found different ξ, ranging from 0.73 to 0.8 [24, 46].

Interestingly in a simulation of a supercooled liquid of dumbbells, it was found that translation-rotation decoupling occurs at the single particle level. They used es-

sentially the same method to determine both D_T and D_R through mean square displacements(Eqns. 1.11,1.12). They observed an enhancement of rotation relative to translation, opposite to previous experiments in OTP.

In fact, a number of experiments and simulations yield different results on the nature of decoupling [39, 42, 47]. One key feature to be noted is that all these simulations have different shaped particles. Recent experiments on ellipsoidal glasses [36] found that longer ellipsoids formed liquid crystal phases, while shorter aspect ratio ellipsoids formed glass-like phases.

As explained in Chapter 4, in our experiments we observe naturally occurring silica dimers embedded in a 2D bidisperse and the experiments are the same as in Chapter. 3. We find that for dimers of smaller lengths, rotations do not slow down as much as translations, on approaching the glass transition, similar to the case of spheres as probes [48]. However we find that in our longest dimers, D_T and D_R remain coupled at all concentrations, i.e. $D_T/D_R \sim$ constant.

Chapter 2

Soap Films as model 2D fluids

2.1 Introduction

Soap films are thin liquid films. These films are stabilized by two surfactant layers on either side. Surfactant molecules stabilize the film as they like to remain at the film-air interface. They have two components - a hydrophilic head and hydrophobic tail.

Soap films have complex hydrodynamics [49] that have been widely investigated as early as the late 19th century for example by Plateau [50] and Gibbs [51]. Previous

Figure 2.1: Soap film drawn between metal wires used in experiments

experiments have demonstrated that thin soap films behave in many respects as two-dimensional (2D) fluids [52–56]. Soap films have applications as a wide range of model systems. For example, soap films share similarities to cell membranes [57]. Soap films were used to study swimming fish and flapping flags in a two dimensional wind [55]. Quickly flowing soap films also served as model systems for 2D turbulence [56, 58, 59], which is relevant in our atmosphere at large scales.

We are interested in understanding soap film hydrodynamics using microrheology, by adding micron sized tracer particles and analyzing their diffusive motion [52–54]. Particle motions in a soap film are constrained in the third direction, due to small film thickness. Hence, their diffusive motion is two-dimensional and controlled by an effective 2D viscosity of the soap film, η_{2D}. η_{2D} is expected to be related to the film thickness and other details of the soap solution using the 1957 Trapeznikov approximation [60]. In 1975 Saffman and Delbrück argued that diffusive motion in a fluid membrane is also influenced by the surrounding three-dimensional (3D) viscous fluids with viscosity η_{3D} on either side of the membrane [11]. In the case of interest to soap films, the surrounding 3D fluid is air with viscosity $\eta_{3D} = \eta_{air}$. The Saffman-Delbrück approximation [7, 11] relates the observable single particle diffusivity D to η_{2D}, η_{air}, and the particle diameter d, allowing one to determine η_{2D} by observing tracer particle trajectories [52].

The Saffman-Delbrück theory is based on modeling a spherical tracer as a cylinder with diameter d and height h. This seems plausible for spheres with $d \geq h$, but it is questionable how sensible this is for spheres with $d < h$. There has only been minimal experimental exploration of this limit [52]. In prior work, it was demonstrated that the Saffman-Delbrück approximation works well up to $h/d = 4$, and is no longer applicable for $h/d \geq 10$ [52]. Unfortunately, these experiments did not have data in the interesting regime $4 \leq h/d \leq 10$. For their thin films $h/d < 4$, they found that diffusive measure-

ments interpreted with the Saffman-Delbrück approximation led to results in agreement with the prediction of Trapeznikov [60] for η_{2D}. Due to the lack of data in the crossover region, it was unclear if the crossover from 2D to 3D behavior was a smooth function of h/d or some other parameter.

In this work, we present new experimental data of the diffusivity of particles in soap films, to examine more closely the breakdown of the cylindrical assumption of the Saffman-Delbrück approximation. In this current work we use a more reliable means of measuring film thickness h and due to experimental improvements are able to get data from a wider range of film thicknesses and particle sizes. While the previous work probed a single d at the crossover, in this work we use particles of two different d and verify that h/d is the correct parameter indicating the crossover. We find that the Saffman-Delbrück model works well up to $h/d < 5.2 \pm 0.9$, and that there is a smooth crossover from thin films to thick films as a function of h/d. We additionally examine the correlated motion of pairs of particles as a function of their separation to independently infer η_{2D}, and in doing so we demonstrate that the Trapeznikov prediction is valid for all soap films, independent of h/d. Our results clarify that this correlated particle motion is a more effective way to measure η_{2D} from observing diffusive motion of tracers in a soap film. While this had been suggested by prior work [52], our results provide a wider range of data in support of the interpretation put forth earlier.

Further background discussion of the Saffman-Delbrück and Trapeznikov approximations is presented in the following section.

2.2 Hydrodynamic theory

Single particle diffusion in thin films

Our starting point for diffusion is to measure the mean square displacement of tracer particles, which is related to the diffusion constant as

$$\frac{\langle \Delta r^2 \rangle}{4\tau} = D_{1p} \tag{2.1}$$

Here τ is the lag time for the displacement, $\Delta r = |\vec{r}(t+\tau) - \vec{r}(t)|$, and the subscript $1p$ indicates that this diffusion constant D_{1p} is based on averages over single particle motion.

In 3D, the single particle diffusion constant relates to the 3D viscosity η_{3D} by the Stokes-Einstein-Sutherland equation [9, 10]

$$D_B = \frac{k_B T}{3\pi \eta_{3D} d}, \tag{2.2}$$

with Boltzmann constant k_B, absolute temperature T, and particle diameter d. The subscript B indicates this is a bulk diffusivity. However, this equation does not apply to soap films, for several reasons. First, as noted previously, 2D fluid flows are fundamentally different than 3D flows, leading to more complex relationships between D_{1p} and d. Second, diffusion and flow in a soap film is influenced by the viscosity of the surrounding air. Third, the viscosity in 2D has different units: Pa·s·m as compared to Pa·s in 3D. In 1975 Saffman and Delbrück treated this case, deriving an approximation for D_{1p} for the situation of a 2D membrane with interfacial viscosity η_{2D} with fluid of 3D viscosity η_{3D} on both sides of the membrane [11]. Using the small parameter $\epsilon = d\eta_{3D}/\eta_{2D}$, Saffman and Delbruck

found [11, 12]

$$D_{1p} = \frac{k_B T}{4\pi\eta_{2D}} \left[\ln\left(\frac{2}{\epsilon}\right) - \gamma_E \right], \tag{2.3}$$

using Euler's constant $\gamma_E = 0.577$. In particular, this derivation treated the 2D membrane as a thin 3D layer of fluid with 3D ("bulk") viscosity η_B, thickness h, and therefore a 2D viscosity $\eta_{2D} = h\eta_B$. They considered the diffusion of disks of diameter d and height h which spanned the membrane thickness, and which only move horizontally (within the membrane). Equation 2.3 works well for small ϵ (large η_{2D}). ϵ^{-1} is often termed the Boussinesq number Bo, so equivalently Eqn. 2.3 works well for large Bo [2, 13]. Hughes *et al.* [14] extended Eqn. 2.3 to work for all ϵ, with a useful approximation to their result added later by others [15, 16]. While the large ϵ limit is of less interest to small particles diffusing in soap films, we note that the large ϵ behavior has been experimentally verified in lipid membranes [16] and liquid crystal films [17]. Note that Eqn. 2.3 assumes that the interface horizontal extent R is sufficiently large ($d/R < \epsilon$), which is the case for us ($R \approx 1$ cm) [11].

Soap films are made from a regular fluid with added surfactant molecules, and it is straightforward that the effective viscosity η_{2D} for a soap film should depend on its constituents. This was first described in 1957 by Trapeznikov [60]. He noted that there should be a contribution $h\eta_B$ from the bulk fluid used to make the soap film. Dimensionally, this makes sense, and it is also physically reasonable that η_{2D} should increase for larger h or η_B. Trapeznikov also noted that the surfactants at the fluid-air interface should themselves act like a 2D fluid and contribute their own 2D viscosity η_{int}, so therefore the effective 2D viscosity of the entire soap film would be given by

$$\eta_{2D,T} = \eta_B h + 2\eta_{int}. \tag{2.4}$$

This then is a prediction that η_{2D} measured using Eqns. 2.1 and 2.3 is equal to $\eta_{2D,T}$. This prediction was confirmed in prior experiments by Prasad and Weeks for thin soap films with $h/d < 7 \pm 3$ [52, 53], but for thicker films diffusion seemed to sense the 3D nature of the film and follow more closely Eqn. 2.2 [53].

Two particle correlated motion in thin films

Two-particle microrheology is an alternative analysis technique that complements measuring single-particle diffusion via Eqn. 2.1 [8, 61]. Conceptually, this examines correlations between the motion of each pair of particles. If our soap films obey 2D hydrodynamics, two-particle correlations should obey 2D hydrodynamic theory [6] in which the correlations decay as $\ln(R)$, where R is the separation between two particles. This is in contrast to the situation in 3D, in which correlations decay as $1/R$ [8].

Specifically, there are four eigenmodes corresponding to pairwise motion in 2D. Two of these modes are parallel motions (+) in the longitudinal (x) direction (⇜⊖ ⇜⊖) and transverse (y) direction (⇞ ⇞). The other two are anti parallel motions (-) along x (⇜⊖ ⊖⇝) and y (⇞ ⇟). These four correlation functions are calculated by:

$$\begin{aligned} D_{x\pm}(R,\tau) &= \langle \frac{1}{2}[x_i(\tau) \pm x_j(\tau)]^2 \delta(R - R_{ij}) \rangle_{i \neq j} \\ D_{y\pm}(R,\tau) &= \langle \frac{1}{2}[y_i(\tau) \pm y_j(\tau)]^2 \delta(R - R_{ij}) \rangle_{i \neq j} \end{aligned} \tag{2.5}$$

Where i and j denote different particles and R_{ij} denotes particle separation. For a purely viscous system, much as $\langle \Delta r^2 \rangle \sim \tau$ (e.g., Eqn. 2.1), these correlation functions also will be proportional to the lag time τ.

Di Leonardo *et al.* proposed a theory [6] based on the two-dimensional Stokes equation. The theory makes several approximations: neglecting stresses from the bounding

fluid (air), neglecting the finite film size (in the lateral dimension), and neglecting inertia. The Oseen tensor is obtained from the two-dimensional Stokes equation from which the four eigenvalues corresponding to the eigenmodes given above can be solved [6]. The solutions find correlations depending on R as:

$$\begin{aligned} D_{x\pm}/\tau &= A \pm B \ln \frac{L}{R} \\ D_{y\pm}/\tau &= A \pm B \left(\ln \frac{L}{R} - 1 \right) \end{aligned} \tag{2.6}$$

with

$$\begin{aligned} A &= 2D_{1p} \\ B &= \frac{k_B T}{2\pi \eta_{2D}}. \end{aligned} \tag{2.7}$$

L is a length scale beyond which the approximation fails, although it can fail for different reasons in different situations. For example, similar to the Saffman-Delbrück approximation, L could be related to the smaller of the system size R and the Saffman length $l_S = \eta_{2D}/2\eta_{3D}$ [6]. To be clear, the results of Eqns. 2.6 are based on a purely 2D model of hydrodynamic correlations, without any 3D fluid present.

Note that in Ref. [6], they assumed $\eta_{2D} = h\eta_B$ for a soap film [6], but it has been demonstrated that $\eta_{2D} = \eta_{2D,T} = \eta_B h + 2\eta_{int}$ is more appropriate for soap films [52]. As can be seen in Eqn. 2.4, $\eta_{2D,T} \approx h\eta_B$ for thick films where h is large, so the distinction only matters for thin films.

In summary, measuring the correlations described in Eqns. 2.9, fitting to Eqns. 2.6, and interpreting the fit parameters with Eqns. 2.7 is another route to measuring η_{2D}. One advantage of this method is that it should be less sensitive to the exact position of small

tracer particles within the film: partially protruding into the air, or fully immersed in the film. Protrusion of a tracer particle into the air certainly affects its single-particle mobility [62], and so using single-particle analysis methods may result in errors in determining η_{2D}. In contrast, the two-particle correlations are measuring long-range hydrodynamic correlations which are insensitive to the local details [8]. Even if one examines correlations between one particle protruding through the soap film surface and a second particle fully immersed in the film, the particular motions due to the local environment of each particle will be uncorrelated, and the long-range correlations should feel only the hydrodynamic effects of the soap film itself (perhaps as modified due to coupling with the air). Also, the two-particle correlation predictions (Eqns. 2.6) do not make any assumptions about the nature of the tracer particles, but focus only on hydrodynamics. Historically, this insensitivity to the tracer details was a key strength and motivation for two-particle correlation techniques in soft matter [8]. In other words, these predictions do not assume that the tracers are embedded cylinders, unlike the Saffman-Delbrück approach. So, these predictions should hold even in the limit of small tracer particles with diameters smaller than the film thickness, $d \ll h$. Another way to see the advantage of the method is that the correlations between two particles separated by a distance R is probing the same hydrodynamics as a particle of size R would see, and this overcomes the concerns of small particle size [8].

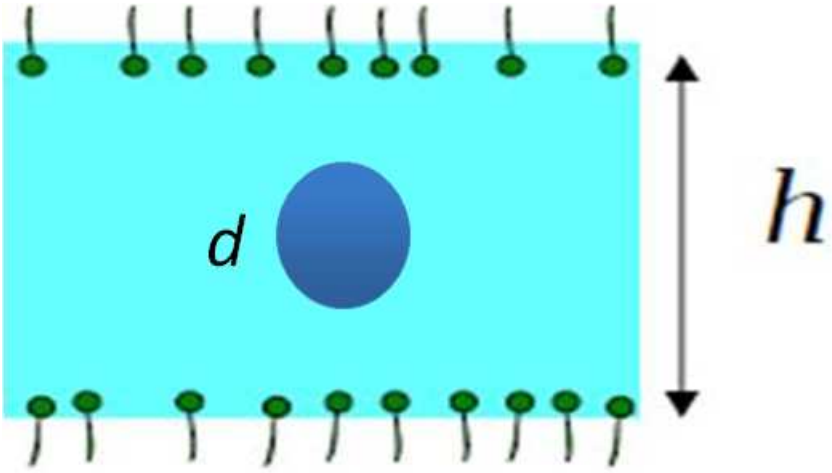

Figure 2.2: Cartoon depicting soap film of thickness h, with a single representative particle of diameter $d < h$. On both air-film interfaces, representative soap molecules are shown. As discussed in the text, we believe it is likely that particles with $d < h$ sit in the interior of the film, but we cannot rule out the possibility that some particles are trapped at the air-film interface.

2.3 Materials and methods

Samples and data acquisition

We make our soap films from bulk solutions of water, glycerol, and surfactant. We use the dishwashing detergent Dawn as our surfactant to stabilize the interfaces of the soap film. Once the bulk solution is prepared, we add fluorescent polystyrene particles of known diameter (we use d=0.1, 0.18, and 0.5 μm). We then draw a soap film from the bulk solution using a rectangular metal wire frame with dimensions $\approx$ 1.5 cm$\times$2.0 cm, and thickness h. A cartoon depicting the film and a representative particle is shown in Fig. 2.2.

We have a microscope chamber made with a water filled sponge lining to increase humidity and reduce evaporation of water from the soap film. This chamber is mounted on our upright microscope, and the freshly drawn soap film is placed inside the chamber.

We seal the chamber as far as possible from outside air, to reduce convection at the soap-film interface.

We use fluorescence microscopy to record a 33 s movie of particles diffusing in the soap film at a frame rate of 30 images/s. The film is illuminated using an arc lamp, and a movie of particles diffusing is taken using a CCD camera. Microscope objectives 20×, 40×, and 63× are used for particles of diameter d=0.5, 0.18, and 0.1 μm respectively. We post-process the movies using particle tracking algorithms [63] to extract particle positions from individual frames. We note that there is position uncertainty from particle localization accuracy. There are multiple ways of measuring this uncertainty [64–66]. We use the CVE method [66] to estimate this uncertainty.

$$\langle \Delta r_n \Delta r_{n+1} \rangle = 4 D_{1p} R \Delta t - 2\sigma^2 \tag{2.8}$$

where n denotes frame number, Δt is the time per frame, $R = 1/6$ is the motion blur coefficient, D_{1p} is the single-particle diffusion coefficient and σ denotes position uncertainty.

The 3 different particle sizes of diameters d = 0.1, 0.18, and 0.5 μm have position uncertainties of 0.10, 0.065, and 0.080 μm respectively.

Some macroscopic flow of the soap film in its frame is unavoidable, resulting in coherent flow of the tracers in our movies. Between each video frame we compute the center of mass motion by finding the average displacement of every particle. The uniform flow is then subtracted from the particle positions to provide their relative locations in the frame of reference co-moving with the flow. This lets us then study the diffusive motion of the individual particles. However, drift removal may artificially reduce true long-range hydrodynamic correlations. We have checked that our algorithm does not unduly affect

the correlations; details of this are given in the Appendix.

We would like to know where our particles are within the soap film, but this is difficult to determine directly given that the depth of focus of our microscope is comparable to the soap film thickness. For particles in films thinner than the particle diameter, it is highly likely that capillary forces ensure that the particle lies symmetrically within the film [67]. One experiment demonstrated that pinning of the contact line at a rough particle surface can sometimes delay reaching the equilibrium position for time scales longer than our experiments [68], and we cannot rule out that our particle positions may not be equilibrated. For particles in films thicker than their diameter, particles might sit at the air-water interface to reduce the air-water surface energy. However, as mentioned in a prior study of soap films [53] and as we observe, small particles in very thick films diffuse as if they are in a bulk solution of the soap film liquid. This would not happen for particles trapped at an interface [62]. The two-particle correlation functions should be less sensitive to the exact positions of the tracer particles. Note that a recent paper showed comparisons between microrheology and macrorheology results, and pointed out that measurements of particles not in the interface are misleading [13]. They were studying cases where the interface was with a bulk liquid and air, quite different from our finite-thickness films. Our particles should still be reporting film properties no matter their location. Our results for the two-particle correlations support this, as will be described in our Results and Discussion section.

Measuring soap film thickness

After taking the movie, we take the film out of the microscope humidity chamber and measure the film's thickness using the infrared (IR) absorption of the water based soap

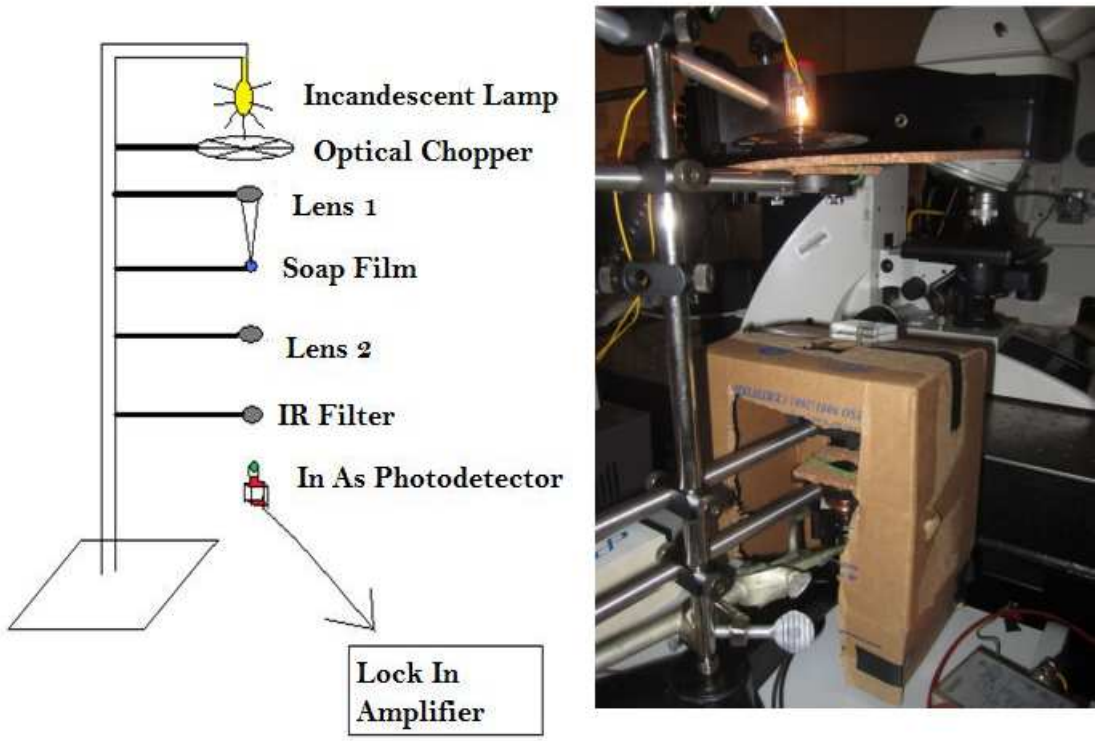

Figure 2.3: Soap film thickness measuring device used in experiments. Light from an incandescent lamp is focused on the soap film. Then the light transmitted from the soap film is incident on the IR filter that allows only light of wavelength 3 μm to be detected by the photodector.

films at wavelength $\lambda = 3.0$ μm. This is based on a previously established technique [69] which we briefly summarize here. Light is incident on the soap film from an incandescent lamp. The light passes through an optical chopper, to chop the light at a particular frequency. This light is then focused on the soap film by an IR lens to a spot size of $\sim$ 2.5 mm. An IR filter (3.00 ± 0.01 μm JML Optical Industries, LLC) in the beam path allows only wavelength of 3.0 μm to pass through. Finally, the light is refocused on an InAs photodiode detector (Teledyne Judson, model J12TE2-66D-R01M) by a second IR lens. The signal from the photodetector is obtained from a lock-in amplifier (Signal Recovery, model 7265) locking with the external reference frequency of the chopper, which reduces noise. We separately measure the refractive index and absorption coefficient of each bulk solution at the same wavelength. From measured transmittance through the film and these details of the bulk solution, we calculate the film thickness using a modified Beer-Lambert law that takes into account the multiple reflections in the soap film. This method is slightly different from prior work [52], and is a notable improvement in that the thickness measurement is done physically adjacent to the microscope and thus is done within 30 s of taking the microscopy data, allowing for higher accuracy. In the prior work of our group, the films often popped before their thickness could be measured. Additionally, there was a lag of several minutes between the microscopy movies and the thickness measurement, which potentially allowed for the film to drain or evaporate and thus increased the uncertainty of those film measurements [52].

Soap films thin over time at the center due to drainage of liquid towards the sides arising from capillary forces. Figure 2.4 shows soap film drainage for 30 percent and 60 percent glycerol weight content soap films. In general, we observe that films made of bulk solutions with lower glycerol concentration drain faster than those made of higher glycerol concentration.

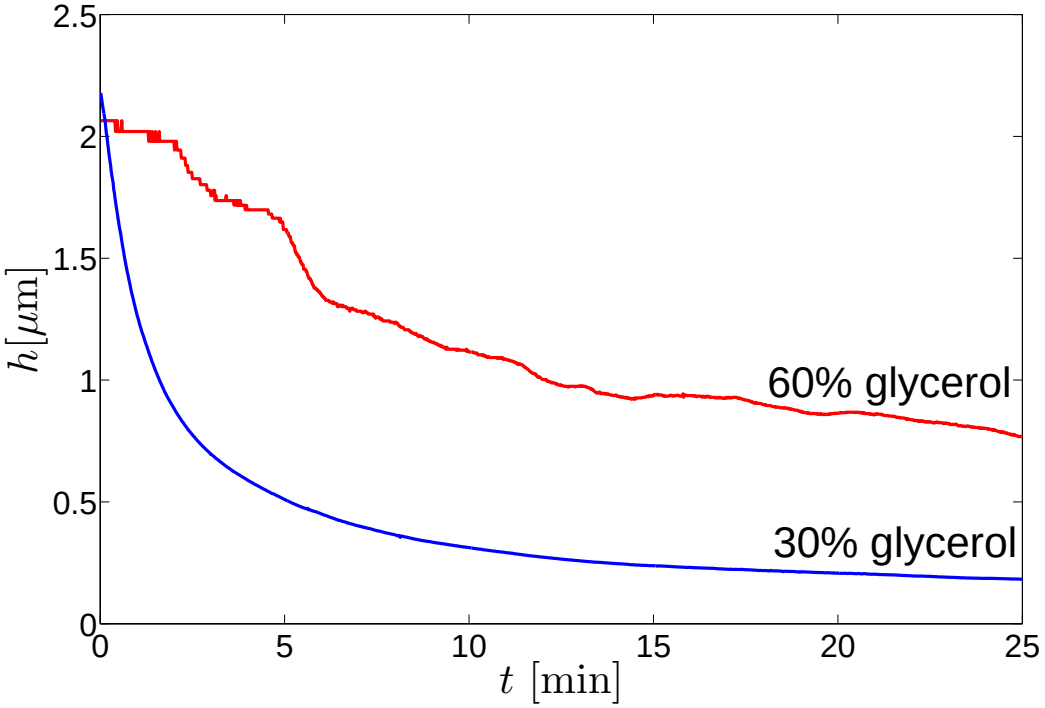

Figure 2.4: Soap film thickness as a function of time which decreases due to soap film drainage, for films with weight percent glycerol as indicated.

The timing of our experiment matters. When the soap film is initially drawn on to our frame, in addition to the drainage, there are also transient flows primarily due to air currents. Accordingly, after placing the film into the microscope chamber and sealing the chamber, we wait for 10 to 20 minutes before taking the movie. This allows the initial rapid drainage to slow, and also the transient flows. The duration of the movie (33 s) and delay before measuring the thickness (30 s) are short on the time scale of the drainage, as is apparent from Fig. 2.4.

In our soap film thickness measurement, there are three main sources of error. The first source of error is due to soap film drainage in the time between our microscopy and soap film thickness measurements. This error is higher in low viscosity soap films due to their faster drainage as mentioned above. We quantify this error by measuring the maximum change in thickness during 30 s from the curves shown in Fig. 2.4, which is a maximum of 0.03 μm. The second source of error comes from the precision of the lock-in amplifier and noise present in the measurement, including possible variations in illumination. This is worse for thicker films (which have less transmitted light) and is at most 0.02 μm. The third source of error is from residual soap film flows and the fact that soap films are not uniformly thick. This error is quantified by the fluctuations in the soap film thickness after long times, when film thickness reaches equilibrium, i.e., when thickness is almost constant. This error is negligible for low viscosity films, but plays an effect in films of higher viscosity, the maximum error being 0.02 μm. We assume these errors are additive. Our maximum error is for the thickest films, which also correspond to the highest viscosities. The maximum uncertainty is ± 0.05 μm.

Effect of drift subtraction on two particle correlation results

Some macroscopic flow of the soap film within the soap film holder is inevitable. This can be quantified by observing that the particles have a slow net drift. That is, $\langle \Delta\vec{r} \rangle = \vec{v}(t)\tau$ with a slowly varying velocity $\vec{v}$, for small lag times τ, and where the angle brackets indicate an average over the displacements $\Delta\vec{r}$ of all particles at a given time. The two-particle correlation functions:

$$\begin{aligned} D_{x\pm}(R,\tau) &= \langle \frac{1}{2}[x_i(\tau) \pm x_j(\tau)]^2 \delta(R - R_{ij}) \rangle_{i \neq j} \\ D_{y\pm}(R,\tau) &= \langle \frac{1}{2}[y_i(\tau) \pm y_j(\tau)]^2 \delta(R - R_{ij}) \rangle_{i \neq j} \end{aligned} \tag{2.9}$$

denote the four eigenmodes corresponding to pairwise motion in 2D. Two of these modes are parallel motions (+) in the longitudinal direction (x) and transverse direction (y). The other two are anti-parallel motions (-) along x and y. By examining the above, it can be seen that such a drift will not affect the anti parallel correlations, but will increase the measured value for the parallel correlation functions D_{x+} and D_{y+}. If $\vec{v}$ was time-independent, then such drift is straightforward to detect and remove from the particle trajectories. However, we often find that $\vec{v}(t)$ has a slow but nontrivial time dependence, and this then makes its influence on D_{x+} and D_{y+} depend on τ. Moreover, due to hydrodynamic interactions, particle motions should have long-range correlations even in the absence of flow, so there is a danger that by removing correlated motion of all the particles, some of the signal from hydrodynamic correlations is lost. As already mentioned, the negative correlations are not affected at all, as they measure the relative displacement of particles, and any center of mass motion cancels out. Likewise, single particle measurements of $\langle \Delta r^2 \rangle$ are barely affected by slow drift; to be safe, we calculate

our single particle data using $\langle(\Delta\vec{r} - \langle\Delta\vec{r}\rangle)^2\rangle = \langle\Delta r^2\rangle - \langle(\Delta r)^2\rangle$.

To deal with the effects of drift on D_{x+} and D_{y+}, we compute $\langle\Delta\vec{r}(t)\rangle$ at every time t using displacements with lag time 1/30 s, the time between images. We then integrate $\langle\Delta\vec{r}(t)\rangle$ to get a trajectory of the center of mass of all of the particles, $\vec{r}(t)$. Next, we smooth this with a running average over T time steps. We then subtract the smoothed $\vec{r}(t)$ from each individual particle trajectory, to bring the individual particle trajectories into the moving reference frame. In some cases we do not do this smoothing, corresponding to the $T = 1$ limit where the center of mass is forced to be motionless once the trajectories are brought into the moving reference frame.

Figure 2.5 shows our analysis of how T affects two particle correlations, for several choices of τ. All values of the smoothing parameter T and lag time τ are given in terms of the frame rate of the camera, so $\tau = 1$ corresponds to 1/30 s for example. We desire that our results should be τ independent ideally. Indeed, as should be, the D_{x-}/τ data all collapse for all smoothing parameters T and lag times τ, as mathematically our procedure leaves the anti parallel correlations unchanged. These are the lower curves in Fig. 2.5 that increase for $R > 2$ μm.

For $T = 1$ in Fig. 2.5(a), the positive correlations D_{x+} have very slight τ dependency, for lower τ. This is likely due to artificial subtraction of positive correlations as explained above. For $T = 8$ in Fig. 2.5(b), the positive correlations at higher $\tau = 8, 12, 16$ almost collapse, with slight τ dependence but the positive correlations curve for $\tau = 4$ is much higher. This is due to lack of drift subtraction for $\tau < 8$ when $T = 8$. This is evidence that $\vec{v}(t)$ changes even on a fairly quick time scale of $\tau = 4$ (corresponding to 4/30 s).

Figure 2.5(c) looks at different smoothing parameters $T = 1, 2, 4, 8$, for the same lag time $\tau = 4$. The curves do not collapse on each other for reasons explained above. Fig. 2.5(d) looks at the same as data (c), but for $\tau = 12$. The curves for different T collapse

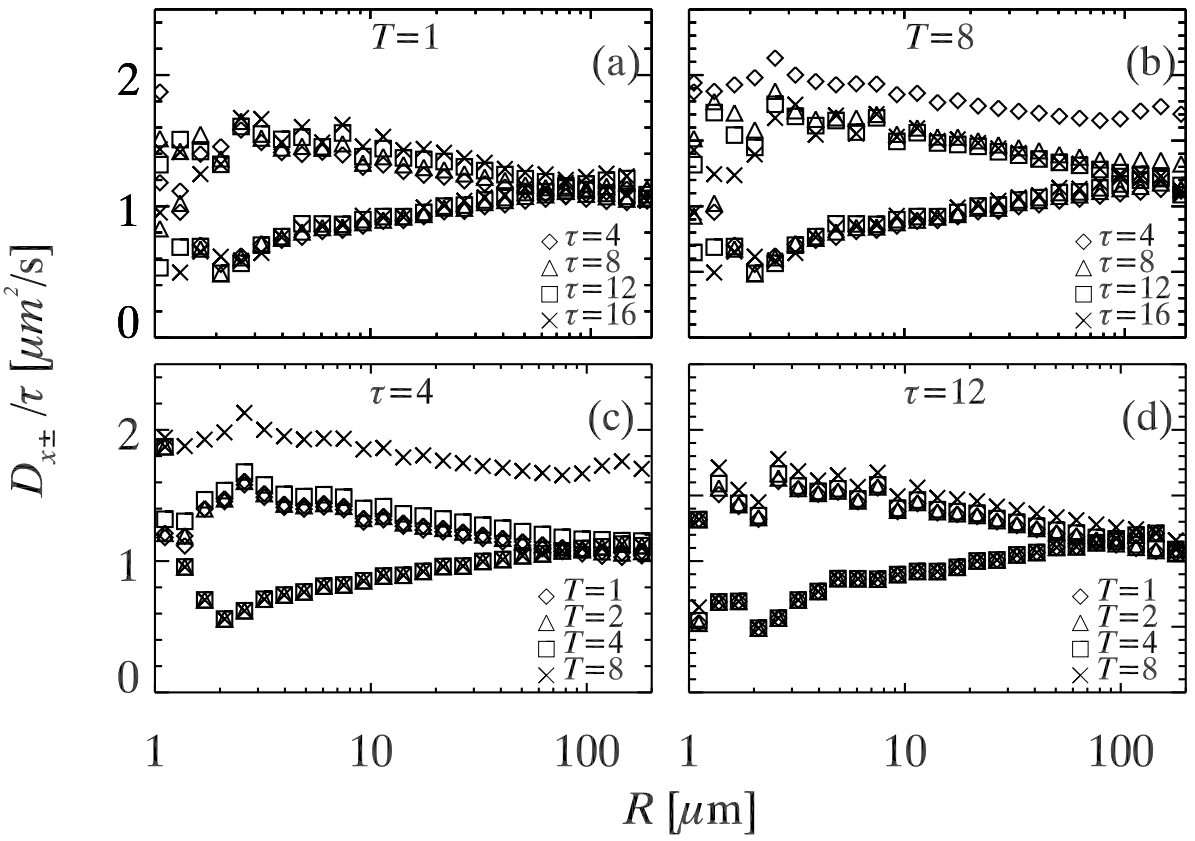

Figure 2.5: (a) shows D_{x+} and D_{x-} for T=1. (b) shows the same data as (a) for $T = 8$. (c) and (d) show D_{x+} and D_{x-} for a particular $\tau = 4, 12$ respectively. Note that T and τ are in units of video frames, where 1 frame = 1/30s.

nicely on top of each other for $\tau = 12$. While the D_{x+} still have very slight dependence, it is much smaller for $T < \tau$. Hence, at higher lag times τs, we are confident that smoothing does not unduly affect our results, as long as the smoothing parameter T is chosen to be shorter than τ. In order for uniform treatment of all samples, we analyze all movies using $T = 1$. For each movie, we average the data over a wide range of τ's. The smallest τ is always 2 video frames (66 ms). The largest τ is chosen for each individual movie to be the largest one for which data are available, in other words, the largest duration over which individual particles are tracked; this is at most 1 s. We compute Eqns. 2.9 for each τ, fit to find the parameters A, B, and L, and then average those parameters over the different τ's. The standard deviations of those data lead to the uncertainties shown in the manuscript. While the evidence of Fig. 2.5 gives support for our choice $T = 1$, we note that there is still some slight τ dependence, causing larger positive correlations corresponding to larger τ. As only the positive correlations are affected, we would expect A to be different as compared to single particle results. However, our results show that this method works well. As noted in the manuscript, we find $A/D_{1p} = 2.02 \pm 0.12$, which is in good agreement with the expected result $A/D_{1p} = 2$.

2.4 Results and Discussion

Single particle diffusion

In the prior soap film studies by our group [52, 53], the single particle diffusion constant was measured through the mean square displacement of tracer particles from Eqn. 2.1 – that is, plotting $\langle \Delta r^2 \rangle$ as a function of τ and fitting a line to find D_{1p}. A recent paper by Vestergaard *et al.* shows that this is not the best method [66]. In the current study, we

use their covariance based estimator (CVE) method. This yields the optimal D_{1p} from

$$\frac{\langle \Delta r_n^2 \rangle}{4\Delta t} + \frac{\langle \Delta x_n \Delta x_{n+1} \rangle}{2\Delta t} + \frac{\langle \Delta y_n \Delta y_{n+1} \rangle}{2\Delta t} = D_{1p} \tag{2.10}$$

Here Δr_n denotes displacement between frames and n denotes frame number. x and y denote the two dimensions, and Δt is the frame rate of recording, 33 ms. The averages are taken over all video frames n and all particles. This method has the advantage of removing fictitious correlations between subsequent frames which can be due to video artifacts or other subtle experimental errors [66].

In a bulk (3D) liquid, diffusivity D_B is a constant given by Eqn. 2.2 [9, 10]. However, in soap films we expect diffusivity D_{1p} to follow Eqn. 2.3 using η_{2D} equal to the Trapeznikov viscosity, $\eta_{2D,T}$ given by Eqn. 2.4. Reversing this logic, we compute η_{2D} from measured single particle diffusivity D_{1p} using Eqn. 2.3, the known viscosity of air ($\eta_{air} =$ 0.017 mPa·s), and the known tracer diameter d. We then obtain η_{int} from this measured η_{2D} via Eqn. 2.4. This interfacial viscosity should be independent of film thickness as it is a property solely of the soap-air interface, and the soap concentration is kept constant throughout our experiments. This conjectured independence is a test of the approximations, and accordingly in Fig. 2.6 we show η_{int} as a function of h/d. Each data point corresponds to a particular soap film. For $h/d < 5$, η_{int} is positive and roughly constant; in this region, the approximations of the Saffman-Delbrück model work well. Taking the mean value of the data for $h/d < 5$ gives us $\eta_{int} = 1.42 \pm 0.74$ n·Pa·s·m. This agrees with a previously published value of 0.97 ± 0.55 n·Pa·s·m for soap films made with the same surfactant [53]. While we do not have a direct method to measure viscosity of the soap-air interface, the rough agreement of the measurements for $h/d < 5$ seen in Fig. 2.6 demonstrate that single-particle diffusivity is one method to measure η_{int} for a soap film,

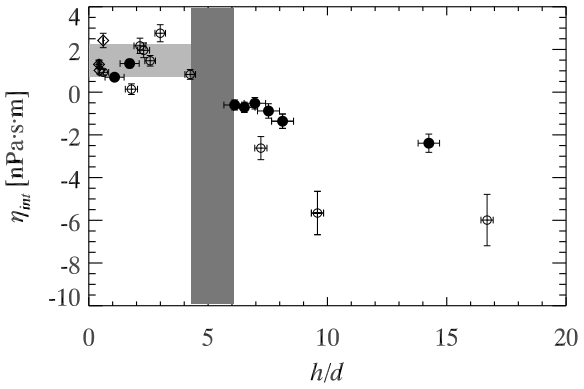

Figure 2.6: Plot of interfacial viscosity from single particle diffusion measurements as a function of h/d. Filled circles denote particles of diameter 0.1 μm, open circles denote particles of diameter 0.18 μm and diamonds denote particles of diameter 0.5 μm. The horizontal light shaded region represents $\eta_{int} = 1.42 \pm 0.74$ nPa·s·m based on the mean and standard deviation of the data for $h/d < 5$. The vertical dark shaded region represents the crossover from physical behavior at small h/d to unphysical behavior at $h/d > 5.2 \pm 0.9$. The horizontal error bars are due to uncertainties of h, and vertical error bars are due to uncertainties of h and η_{2D} (see Eqn. 2.4).

as has been argued previously [53].

Figure 2.6 also shows that for larger h/d, η_{int} is unphysically negative and also quite variable. The crossover occurs at $h/d = 5.2 \pm 0.9$. This value is obtained from the gap in our data in the crossover region, i.e. 5.2 denotes the center of the gap with a width of 0.9 on either side. Our current observation is an improvement over prior experiments which had a larger gap and identified the crossover as $h/d = 7 \pm 3$ [52]. Furthermore, the reasonable agreement for this crossover location between the different particle sizes (different symbols in Fig. 2.6) is good evidence that the crossover is indeed a function of h/d. As noted in the Hydrodynamic theory section, a breakdown for large h/d is expected. The Saffman-Delbrück approximation treats the tracer as a cylinder with height equal to the film thickness, which is dubious for $h/d > 1$. Given that, it is remarkable that this approximation holds up to $h/d = 5.2 \pm 0.9$. Another way to state that is, given our

experimental uncertainty, we see no deviations from 2D behavior up to $h/d = 4.3$.

For larger h/d, the interfacial viscosities in Fig. 2.6 are unphysically negative, showing that particles are diffusing faster than expected – that is, faster than one expects, if η_{2D} were equal to $\eta_{2D,T}$. We also observe that particles of smaller diameter are less negative in Fig. 2.6. This is because for large h/d, particles diffuse more like in bulk [70], i.e., measured diffusion $D_{1p} \approx D_B$, as in Eqn. 2.2. Equating this D_{1p} to the Saffman-Delbrück equation Eqn. 2.3 and approximating the ln term as a constant, we get for large h/d that the measured $\eta_{2D} \sim \eta_B d$. Using Eqn. 2.4 to extract η_{int} from these apparent η_{2D} values, we see that the particular negative values for η_{int} will be smaller in magnitude for smaller d, and that the specific values will also depend on η_B (which differs from film to film in our experiments). The differing d and η_B give rise to the scatter of the data seen in Fig. 2.6 for $h/d > 5.2$. Despite the scatter, it is apparent that there is a fairly smooth crossover from the regime where the Saffman-Delbrück approximation works to where it fails.

Two particle correlated motion

The two-particle measurements should not suffer from the difficulties the one-particle measurements have, as the two-particle correlations reveal the long-range hydrodynamic correlations of a soap film rather than the diffusive properties of a single particle. As described by Eqns. 2.9, we compute the two-particle correlation functions for a particular experiment and plot them in Fig. 2.7 averaging over a wide range of lag times τ. The data behave as expected. For example, for nearby particles (small R), particles move in similar directions and the parallel correlations are large (D_{x+} and D_{y+}, indicated by the solid symbols). The anti parallel motions are smaller for small R (D_{x-} and D_{y-},

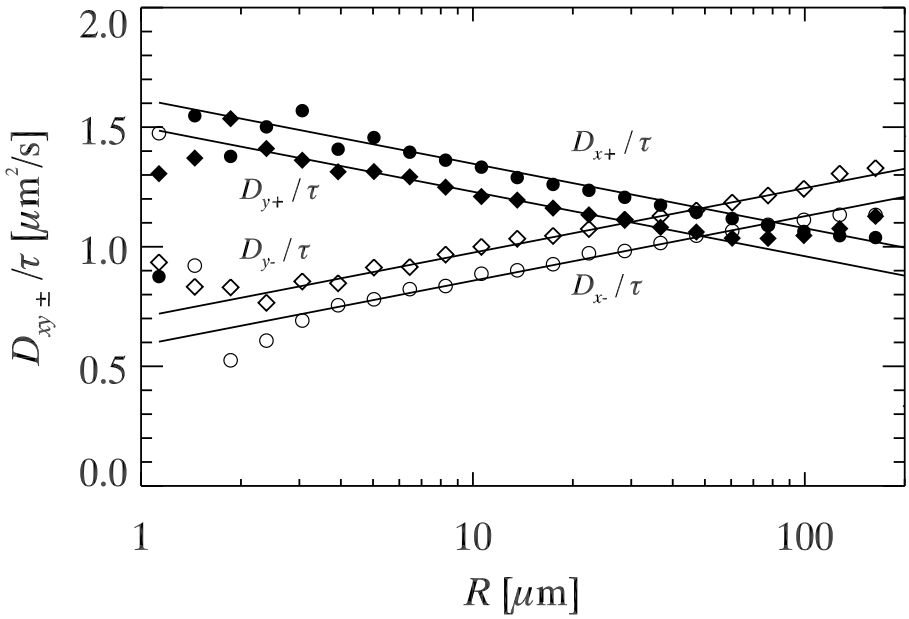

Figure 2.7: Two particle correlations in a single soap film measurement as a function of particle separation R. Particles of diameter $d = 0.18\ \mu m$ were used, and soap film thickness was $h = 0.46 \pm 0.04\ \mu m$. The solid lines are fits from Eqn. 2.6 with $A = 1.09$ μm$^2/s$, $B = 0.12\ \mu$m$^2/s$ and $L = 81\ \mu$m. The data are computed from all particle pairs and averaging over a wide range of lag times τ.

indicated by the open symbols). All of the correlation functions vary logarithmically with R, and Eqns. 2.6 fit the data well as seen by the lines. These lines have three fitting parameters, A, B, and L, which have a simple graphical interpretation. A denotes the point of intersection of positive and negative correlations on the vertical axis, B is the slope of the lines, and L is the point of intersection of D_{x+} and D_{x-} on the R-axis.

For each experimental movie, we compute Eqns. 2.9 as a function of τ, and fit data for each τ to determine coefficients $A(\tau), B(\tau)$, and $L(\tau)$. These have a slight τ dependence, but minimal enough that we simply average over several exponentially-spaced values of τ; see Sec. 2.3 for further discussion. We refer to the τ-averaged values as A, B, and L for the remainder of this paper. We plot these fit parameters in Fig. 2.8 as a function

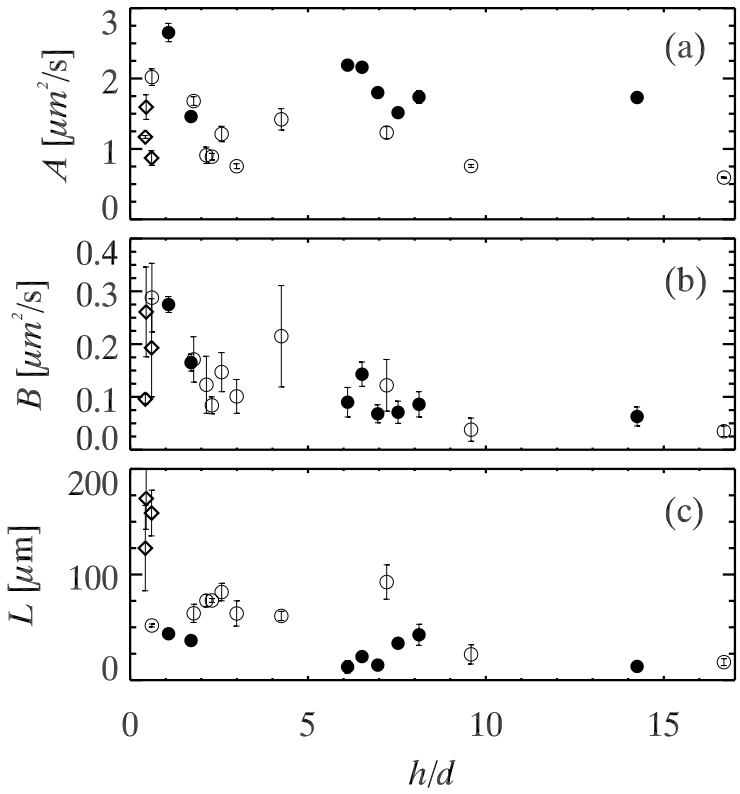

Figure 2.8: Fit parameters for all experiments as a function of h/d. Two particle correlations in a single soap film measurement. Symbols denote particle diameters as in Fig. 2.6. See Eqns. 2.6 and 2.7 for the meaning of the fit parameters. The vertical error bars are from the standard deviations of each fit parameter calculated for the different τ's.

of h/d. The effects of collective drift subtraction on our results are discussed in detail in Sec. 2.3. The uncertainties are reflected by the error bars shown in Fig. 2.8. The data are scattered, which is to be expected as the parameters depend on far more than h/d. The different data correspond to a variety of bulk viscosities and particle sizes. Accordingly, we rescale each of these to make sense of their behavior, and show the rescaled results in Fig. 2.9. We now discuss these rescaled results.

From Eqn. 2.7, we expect $A = 2D_{1p}$ where D_{1p} is the single particle diffusivity of that measurement. Figure 2.9(a) shows A/D_{1p} is constant with value 2.02 ± 0.12, in great

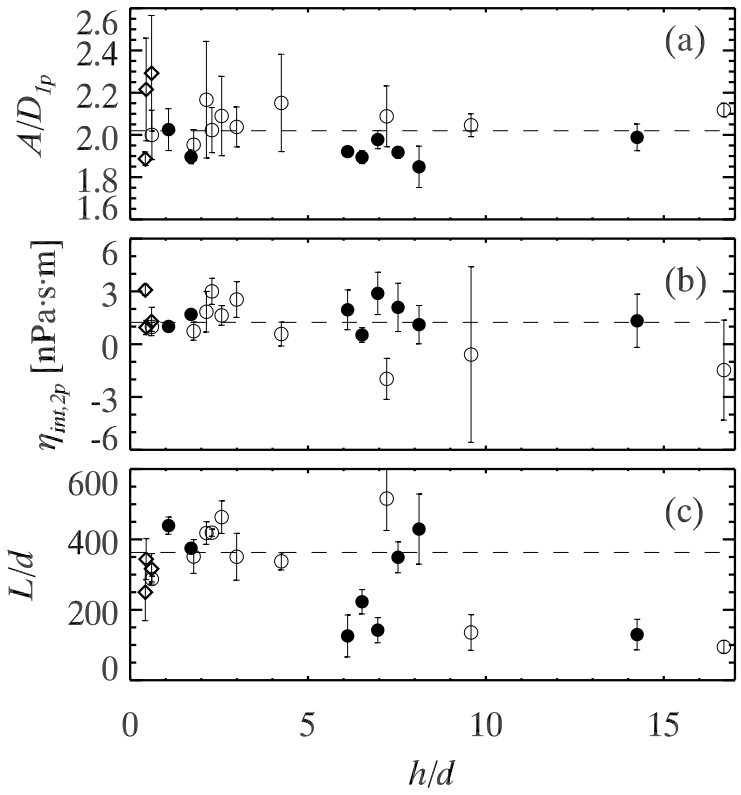

Figure 2.9: Fit parameters for all experiments as a function of h/d. Symbols denote particle diameters as in Fig. 2.6. (a) $A/2D_{1p}$ is roughly constant, with mean value 2.02 ± 0.12 over all data as indicated by the dashed line. (b) $\frac{1}{2}[\frac{k_B T}{2\pi B} - \eta_B h]$, which should theoretically be η_{int}. The dashed line shows the mean value $\eta_{int,2p} = 1.20 \pm 1.30$ nPa·s·m. (c) L/d, where the dashed line represents the mean value $L/d = 360 \pm 60$ for the data with $h/d < 5.2$.

agreement with the theoretical prediction. Previous work by Prasad and Weeks found a value of 1.9 ± 0.1, a moderately concerning discrepancy from the theoretical prediction. The improvement in our current results is due to the CVE method we now use to measure D_{1p} [66]. If we instead use the prior method of fitting a line to $\langle \Delta r^2 \rangle$ we find the erroneous result $A/D_{1p} = 1.83 \pm 0.09$, in agreement with the earlier concerning result.

Figure 2.9(b) shows $\frac{1}{2}[\frac{k_B T}{2\pi B} - \eta_B h]$. This quantity should be the interfacial viscosity η_{int} as seen by rearranging Eqn. 2.7. Hence, this is a method to find the interfacial viscosity from two particle correlations. Averaging all the data in Fig. 2.9(b), we find $\eta_{int,2p} = 1.20 \pm 1.30$ nPa·s·m. This is consistent with our single particle measurement ($\eta_{int,1p} = 1.42 \pm 0.74$ nPa·s·m). While the two-particle measurement has a larger uncertainty, we believe the two-particle value to be more reliable as it uses data from all soap films, both thick and thin. Moreover, this two-particle measurement is robust to concerns about the particle position within the film, as previously discussed. Our value of A should depend on the tracer details as it should be tied to D_{1p} through Eqn. 2.7, but B and thus η_{int} should be measuring true properties of the soap film.

Interestingly, rescaling the third fit parameter L by the particle diameter d plausibly collapses the data, especially for small h/d, as shown in Fig. 2.9(c). For thin films ($h/d < 5$), $L/d = 360 \pm 60$, indicated by the dashed line. For thicker films L/d shows scatter and for the most part is smaller than the thin film value.

Di Leonardo *et al.* [6] discuss the possible origins of the length scale L. In a purely theoretical infinite-extent planar 2D fluid, there is no cutoff length scale L, and correlations die out at infinity. In reality, the finite system size provides one potential cutoff length scale, which was the case in their work with small films. Our film boundary is at least 500 μm away from our field of view, so this seems unlikely to explain our values of L of the order of 10-200 μm. Particle motion relative to the film can lead to another

length scale [2, 6, 7], but our particles are passive tracers (in contrast to Ref. [6] for example, which used laser tweezers to move particles). Another possibility is stresses from the surrounding air [2, 6, 7], which cannot be neglected at distances larger than the Saffman length l_s. In our system, $l_s = \eta_B h/2\eta_{air}$, which varies from $10 - 1000\mu$m. However, our observed L does not have such a wide range. Furthermore, our thicker films generally have higher η_B than thinner films, and hence larger l_s, yet have smaller values of L. None of these length scales seem to match our observed L, and these possibilities do not explain our observed dependence of L on particle size d. Another possible candidate is the capillary interactions between particles. Previous studies found that capillary interactions between particles in a freely suspended liquid film can cause particle-particle interactions even at distances greater than 100μm [67, 71, 72], and these interactions should scale with d. These forces would depend on if particles penetrate zero, one, or two of the film-air interfaces, but capillary forces should not otherwise depend on the film thickness, so the variability seen in Figs. 2.8(c) and 2.9(c) as h/d changes seems to contradict this. Additionally, as explained in the Materials and methods section, in thick films we think our particles are likely to be in the film interior – not penetrating either film-air interface – and thus not experiencing capillary forces. One final possibility is that the theory [6] takes only two particles into account. We typically observe $O(50)$ particles in a field of view, and perhaps many body effects are present in our data. These might affect L by screening particle-particle correlations. These effects however are more complicated to model, and determining a length scale due to many-body effects is not possible. Moreover, our data are from a variety of concentrations all in the fairly dilute limit, and concentration variations seem not to explain the behavior of L.

2.5 Conclusions

We have used two different methods for measuring the effective two-dimensional viscosity η_{2D} of a soap film. The 1957 paper by Trapeznikov [60] put forth Eqn. 2.4 conjecturing that this viscosity is related to the soap film thickness, the viscosity of the fluid used to form the film, and a contribution from the surfactant layers bounding the film; in other words, $\eta_{2D} = \eta_{2D,T}$. As we have used the same surfactant concentration for all of our soap films, the validation of our methods for measuring η_{2D} is the consistency between different measurements of η_{int}, the contribution to η_{2D} from the surfactant layers. Figure 2.6 shows that for single-particle measurements, we can get plausible values of η_{int} for thin films only. Figure 2.9(b) shows that using two-particle correlations, we get moderately consistent values of η_{int} from all of our measurements. The scatter of the data in both of these figures shows that neither of these methods are fool-proof, and best results are obtained by averaging over many films. On the other hand, given the variability of our tracer particle size (a factor of 5), bulk viscosity of the soap film solutions (a factor of 4), and film thicknesses h (a factor of 30), the agreement of the η_{int} data is encouraging. Our measurement of $\eta_{int} = 1.20 \pm 1.30$ nPa·s·m based on the two-particle correlations is the value we have the most confidence in, as it uses data from every experiment we have done and is least dependent on the details of the tracer particles.

For larger soap films, the one-particle data of Fig. 2.6 show unphysically negative η_{int} values, whereas for the two-particle results the data are generally physically plausible [Fig. 2.9(b)]. The one-particle data are due to the breakdown of the assumptions behind the Saffman-Delbrück model, which models the tracers as cylinders which span the soap film thickness. Given this, it is pleasantly surprising that the Saffman-Delbrück approach works for films up to four times thicker than the spherical particle diameter.

The two-particle method, in contrast, does not depend on the details of the tracers as sensitively, but rather on the long-range hydrodynamic properties of the soap film as a two-dimensional fluid. That these hydrodynamic properties indeed behave in a two-dimensional manner is demonstrated in Fig. 2.7 where the two-dimensional theory fits through the data.

These methods for measuring η_{2D} and η_{int} should be useful for measuring the shear viscosities of other surfactants. Our confirmation that the flow fields are two-dimensional in character on length scales of $5 - 100$ μm are a useful complement to prior macroscopic experiments that treated soap films as two-dimensional fluids [55, 56, 58, 59]. In summary, the diffusive motion of particles appears quasi-two-dimensional for thin films but not for thick films, whereas the long-range flow fields appear quasi-two-dimensional for both thick and thin films.

Chapter 3

The 2D vs 3D glass transition in colloids

3.1 Introduction

If a liquid can be cooled rapidly to avoid crystallization, it can form into a glass: an amorphous solid. The underlying cause of the glass transition is far from clear, although there are a variety of theories [25–27]. One recent method of understanding the glass transition has been to simulate the glass transition in a variety of dimensions (including 4 dimensions or higher) [33, 34, 73–75]. Indeed, the glass transition is usually thought to be similar in 2D and 3D [30, 32] and in simple simulation cases such as hard particles, one might expect that dimensionality plays no role. As a counterargument, two-dimensional and three-dimensional fluid mechanics are qualitatively quite different [76]. Likewise, melting is also known to be qualitatively different in 2D and 3D [21–23, 77].

Recent simulations give evidence that the glass transition is also quite different in 2D and 3D [33–35]. In particular, Flenner and Szamel [33] simulated several different

glass-forming systems in 2D and 3D, and found that the dynamics of these systems were fundamentally different in 2D and 3D. They examined translational particle motion (motion relative to a particle's initial position) and bond-orientational motion (topological changes of neighboring particles). They found that in 2D these two types of motion became decoupled near the glass transition. In these cases, particles could move appreciable distances but did so with their neighbors, so that their local structure changed slowly. In 3D, this was not the case; translational and bond-orientational motions were coupled. They additionally observed that the transient localization of particles well known in 3D was absent in the 2D data. To quote Flenner and Szamel, "these results strongly suggest that the glass transition in two dimensions is different than in three dimensions."

In this work, we use colloidal experiments to test dimension dependent dynamics approaching the glass transition. Colloidal samples at high concentration have been established as model glass formers [28–31]. Colloidal experiments have the advantage that individual particles can be visualized. We analyze three different types of colloidal samples, all using bidisperse mixtures to avoid crystallization.

We perform experiments with two 2D bidisperse systems, one with with quasi-hard interactions, and the other with long range dipolar interactions. The first sample type is a quasi-2D sample with hard particles (short range, purely repulsive interactions) which we term '2DH.' The 2DH sample is made by allowing silica particles to sediment to a monolayer on a cover slip [78]. The second sample type is also quasi-2D but with softer particles, which we term '2DS.' The 2DS system is composed of bidisperse PMMA particles dispersed in oil, at an oil-aqueous interface [79].

3D data are obtained from previous experiments by Narumi *et al.* [80] which studied a bidisperse mixture of hard particles. Our results are in qualitative agreement with the simulations of Flenner and Szamel.

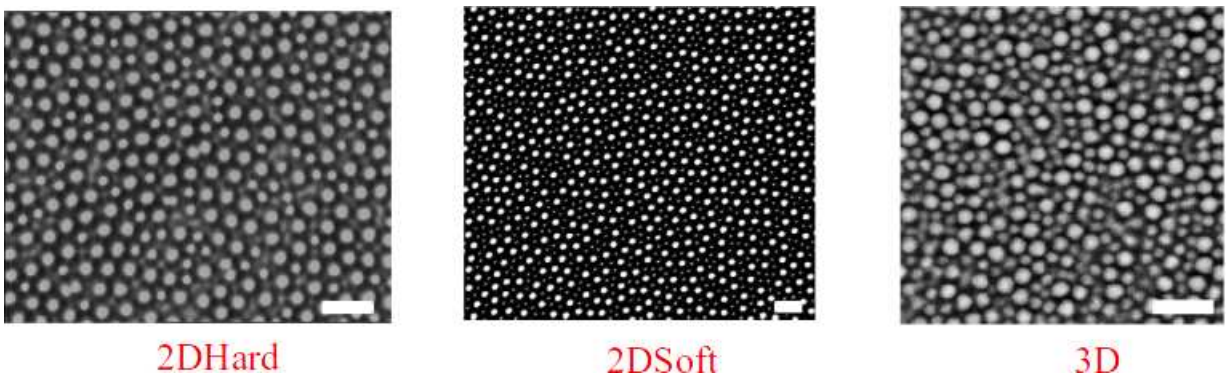

Figure 3.1: Images of 2DH, 2DS, and 3D samples. Scale bar denotes 10 μm.

We believe our observations are due to the Peierls instability [18, 81], also called Mermin-Wagner fluctuations [19, 82]. As Peierls originally argued, there exist long-range thermal fluctuations in positional ordering in one-dimensional and two-dimensional solids. Illing recently noted that these arguments should apply to disordered systems as well [83]. One can measure particle motion relative to the neighbors of that particle to remove the influence of these long wavelength fluctuations [84]. Using this method we observe that the translational and structural relaxations are similar between 2D and 3D, demonstrating that the underlying glass transitions are unaffected by the Mermin-Wagner fluctuations.

3.2 Materials and Methods

For 2D Hard (2DH) experiments, we confine bidisperse non-functionalized silica particles (diameters $\sigma_S = 2.53$ and $\sigma_L = 3.38$ μm, Bangs Laboratories, SS05N) to a monolayer by gravity. The number ratio is $N_L/N_S = 1.3 \pm 0.5$, and varies from sample to sample. The particles are confined between a coverslip and a glass slide, at the coverslip interface for microscopy. The coverslip is made hydrophobic by treatment with Alfa Aesar Glassclad 18 to prevent particle adhesion. All particles are observed to move during the experiment;

none adhere to the glass. We do not add salt. Prior to taking data, the sample is quenched by shaking and letting particles sediment on the coverslip (effectively, this is a concentration quench). The sedimentation lengths ($l_g = k_BT/F_g$) for both small ($l_g/\sigma_S = 0.019$) and large particles ($l_g/\sigma_L = 0.006$) are small enough to ensure fast sedimentation and formation of a quasi-2D monolayer; that is, thermal energy is not enough to overcome the gravitational potential energy of the particles [30]. We verify that in all experiments, only one layer of particles is present (ensured by keeping the overall particle concentration below the level that requires a second layer to form). We use brightfield microscopy and a CCD camera to record movies of particles diffusing. This system is analogous to 2D hard disks. The only caveat is that the centers of the large and small particles are not at the same height, so adjacent large and small particles do not contact each other at their midplane [85]. This allows these two particle sizes to come slightly closer together than they would otherwise, perhaps enhancing the disorder similar to the Kob-Andersen binary Lennard-Jones mixture [86].

For 2D Soft (2DS), the experimental system is composed of bidisperse poly(methyl methacrylate) (PMMA) colloids of diameters 1.1 and 2.6 μm. The particles are at the interface between oil and a glycerol/water mixture. The aqueous phase consists of 10mM NaCl 70 wt. % glycerol solution, while the oil phase consists of a 50-30-20 v/v mixture of cyclohexyl bromide, hexane and dodecane. Interactions between particles are dipolar in the far-field limit. A dimensionless interaction parameter [31] is used to characterize the system:

$$\Gamma_{2DS} = \frac{(\pi n)^{3/2}}{8\pi\epsilon k_B T}(\xi p_B + (1-\xi)p_A)^2 \tag{3.1}$$

where $\epsilon = 4.2\epsilon_0$. The electric dipole moments are p_A and $p_B = 2300$ and 590 $e \cdot \mu$m respectively. $\xi \approx 0.57 - 0.83$ is the number fraction of small particles, and n is the areal

density, measured from a Voronoi tessellation.

The 3D sample data were obtained from a previous experiment by Narumi *et al.* [80]. In 3D experiments, PMMA colloids were stabilized sterically by a thin layer of poly-12-hydroxy-stearic acid. A binary mixture with diameters $\sigma_L = 3.10$ μM and $\sigma_S = 2.36$ μm were used. The number ratio of small particles to large particles was 1.56.

The imaging regions encompass roughly 400, 1500, and 2000 particles for 2DH, 2DS, and 3D samples respectively at their highest concentrations. The total system sizes are much larger, approximately $10^5 - 10^6$ for both 2D systems and 10^9 for the 3D system. We post-processed 2DH and 2DS movies using particle tracking algorithms [63] to extract particle positions from individual frames. The 3D data were previously tracked using the same algorithm. Our uncertainty in particle position is 0.1 μm for the 2DH experiment, 0.5 μm for the 2DS experiment, and 0.2 μm (x, y) and 0.3 μm (z) for the 3D experiment [80].

The α relaxation timescales are computed from self-intermediate scattering functions: $F_S(k, \Delta t) = \langle \exp(i\vec{k}\cdot\Delta\vec{r})\rangle_t$ where $\Delta\vec{r} = \vec{r}(t+\Delta t) - \vec{r}(t)$. The wave vector k corresponds to the peak of the structure factor $S(\vec{k}) = \langle N^{-1}|\sum_{i=1}^{N}\exp(i\vec{k}\cdot\vec{r_i}(t))|^2\rangle$, where $\vec{r_i}(t)$ denotes particle positions at time t and the average is over all times. Corresponding to 2DH, 2DS, and 3D, $k = 2.2, 1.0$, and 2.6 μm^{-1}, obtained using the average k across all samples of a particular type.

Several other functions we compute require identifying nearest neighbors. For both 2D and 3D, for all functions below we use the Voronoi tessellation to identify the neighbors [29].

We define cage relative translational correlation function as: $F_{S-CR}(k, \Delta t) = \langle \exp(i\vec{k}\cdot\Delta\vec{r}_{CR})\rangle_t$ where $\Delta\vec{r}_{CR} = \vec{r}(t+\Delta t) - \vec{r}(t) - \frac{1}{N}\sum_j[\vec{r_j}(t+\Delta t) - \vec{r_j}(t)]$, where j denotes nearest neighbors of the particle at initial time t, and the sum is over all neighbors. The cage

relative mean square displacement is defined using the same displacements $\Delta\vec{r}_{CR}$. To measure bond-orientational correlations in 2D [33], we define $\Psi_6^n(t) = \sum_m (N_b^n)_m^{-1} e^{i6\theta_m}$, where m are the nearest neighbors of particle n and θ_m is the angle made by particle m with defined axis. From this, the bond-orientational correlation function can be found as $C_\Psi(\Delta t) = \langle \sum_n [\Psi_6^n(t)]^* \Psi_6^n(t+\Delta t)\rangle_t / \langle \sum_n |\Psi_6^n(t)|^2 \rangle_t$.

In 3D, we define $Q_{lm}^i(t) = (N_b^i)^{-1} \sum_j q_{lm}[\theta_{ij}(t), \phi_{ij}(t)]$ where $q_{lm}(\theta, \phi)$ are spherical harmonics [33, 87] and the sum is over neighbors of particle i. Next we define the correlation function $Q_l(t_1, t_2) = 4\pi/(2l+1) \sum_i \sum_{m=-l}^{l} Q_{lm}^i(t_2)[Q_{lm}^i(t_1)]^*$. We calculate $C_Q(\Delta t) = \langle Q_6(t, t+\Delta t)\rangle_t / \langle Q_6(t,t)\rangle_t$ corresponding to $l = 6$, given that $l = 6$ is sensitive to hexagonal order known to be present even in disordered samples.

The two-particle vector correlations are determined from a spatial-temporal correlation function defined as $S_{\text{vec}}(R, \Delta t) = \langle \vec{\Delta r}_i \vec{\Delta r}_j \rangle_{\text{pair}} / \langle (\vec{\Delta r}^2) \rangle$ [32, 88]. The average is over all particles with initial separation $R \approx d$, and over the initial time t. For the initial separation R, we use $R = 3.38 \pm 0.2$, $R = 6.5 \pm 0.4$, and $R = 3.1 \pm 0.2$ μm for the 2DH, 2DS, and 3D data. To determine the displacements $\Delta\vec{r}$ we use the time scale Δt such that $F_S(\Delta t) = 0.5$. This is chosen to be a shorter time scale than τ_α, as particle displacements are typically maximally spatially heterogeneous at a shorter time scale [29, 89].

For simulations, we used Lennard-Jones potential in systems evolving with Newtonian dynamics in an NVT ensemble. The simulations were performed using LAMMPS [90].

In 2D we simulated a 65:35 binary mixture of Lennard-Jones particles [91]. In 3D we simulated a 80:20 binary mixture same as in [86]. The interaction potentials are the same in 2D and 3D, given by

$$V_{\alpha\beta}(r_{ij}) = 4\epsilon_{\alpha\beta} \left[\left(\frac{\sigma_{\alpha\beta}}{r_{ij}} \right)^{12} - \left(\frac{\sigma_{\alpha\beta}}{r_{ij}} \right)^{6} \right] \tag{3.2}$$

where r_{ij} is the distance between particle i and j, and α and β denotes the type of particle. We denote the majority species as the A particles and the minority species as the B particles; the potential parameters are given by $\epsilon_{BB} = 0.5\epsilon_{AA}$, $\epsilon_{AB} = 1.5\epsilon_{AA}$, $\sigma_{BB} = 0.88\sigma_{AA}$, and $\sigma_{AB} = 0.8\sigma_{AA}$. We present results in reduced units, where the unit of length is σ_{AA} , the unit of temperature is k_B/ϵ_{AA} , and the unit of time is $\sqrt{(}m\sigma_{AA}^2/\epsilon_{AA})$. The mass for both species are the same. We simulated N = 10000 particles in 2D and 1000 particles in 3D at T = 1.0, 0.8, 0.6, and 0.5. For 2D the number density is 1.2, same as in [91]. In 3D we used a cubic box of length $9.4\sigma_{AA}$ and hence number density 1.2, same as in [86].

3.3 Results

We analyze three different types of colloidal samples, all using bidisperse mixtures to avoid crystallization. The first sample type is a quasi-2D sample with hard particles (short range, purely repulsive interactions) which we term '2DH.' The 2DH sample is made by allowing silica particles to sediment to a monolayer on a cover slip [78]. Our 2DH system is analogous to a 2D system of hard disks of the sort studied with simulations [92, 93]. The control parameter is the area fraction ϕ, with glassy samples found for $\phi \geq \phi_{g,2DH} = 0.79$.

The second sample type is also quasi-2D but with softer particles, which we term '2DS.' The 2DS system is composed of bidisperse PMMA particles dispersed in oil, at an oil-aqueous interface [79]. The interactions in this system are dipolar in the far-field limit, and the control parameter is the dimensionless interaction parameter Γ_{2DS}, related to the area fraction. Γ_{2DS} is defined in the Methods section, with glassy behavior found for $\Gamma \geq \Gamma_{g,2DS} = 530$. For the third sample type, '3D,' we use previously published 3D data on a bidisperse sample of hard-sphere-like colloids [80]. For these data, the control

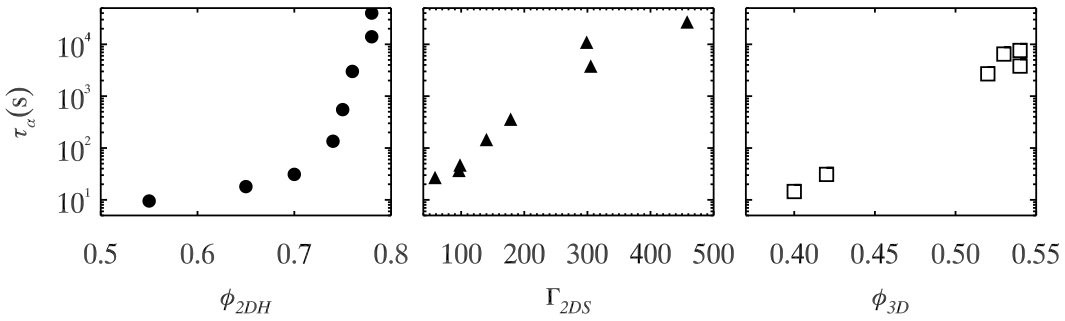

Figure 3.2: Alpha relaxation timescale τ_α v/s concentration parameters of 2DH, 2DS, and 3D samples. Left: 2DH sample data, glassy behavior for $\phi \geq \phi_g = 0.79$. Middle: 2DS sample data, glassy behavior for $\Gamma \geq \Gamma_{g,2DS} = 530$. Right: 3D sample data, glassy behavior for $\phi \geq \phi_g = 0.58$.

parameter is the volume fraction ϕ with glasses found for $\phi \geq \phi_g = 0.58$ [80]. Details of the sample preparation and data acquisition for these three sample types are in the Methods section. For each sample type the glass transition is defined as the parameter (Γ or ϕ) above which the sample mean square displacement (MSD) does not equilibrate in experimental time scales, $\sim$ 10 hours for the 2D samples and $\sim$ 3 hours for the 3D samples.

Flenner and Szamel found that in 2D particles move large distances without significantly changing local structure [33]. They noted that time scales for translational motion and time scales for changes in local structure were coupled in 3D, but not in 2D. The standard way to define these time scales is through autocorrelation functions. Following Ref. [33], we compute the self-intermediate scattering function $F_S(k, \Delta t)$ to characterize translational motion, and a bond-orientational correlation function $C(\Delta t)$ to characterize changes in local structural configuration (see Methods for details). These are plotted in Fig. 3.3$A - C$ and 3.3$D - F$ respectively. At short time scales, particles have barely moved, and so both of these correlation functions are close to 1. At longer time scales these functions decay, taking longer time scales to do so at larger concentrations. The

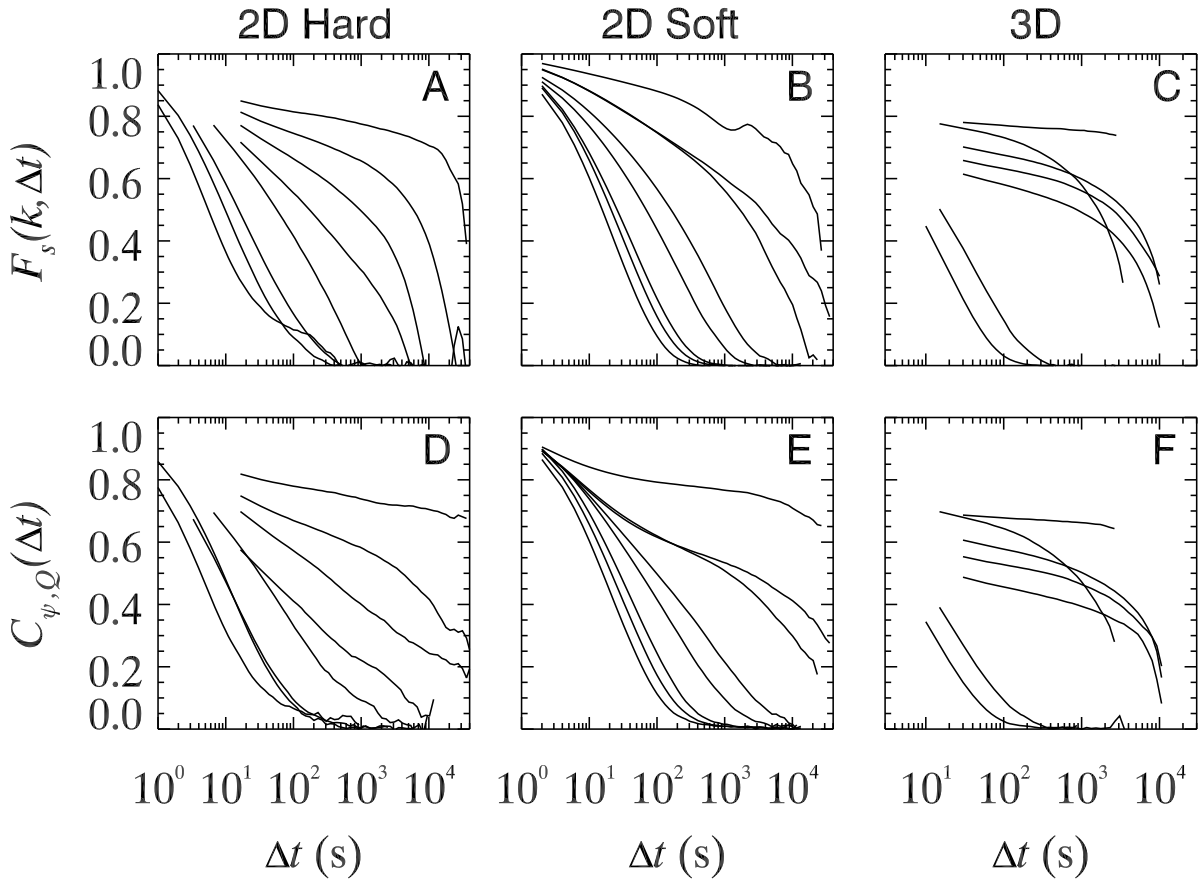

Figure 3.3: Structural relaxation in two and three dimensions. (*A-C*) Self-intermediate scattering functions characterizing translational motion, using the wave vector k corresponding to the peak of the structure factor (see Methods and Materials). (*D-F*) Bond-orientational correlation functions. The columns correspond to 2DH, 2DS, and 3D experiments. The parameters for the experiments are: $\phi_{2DH} = 0.55, 0.65, 0.70, 0.74, 0.75, 0.76, 0.78$, and 0.78; 2DS ($\Gamma_{2DS} = 60, 100, 100, 140, 180, 310, 300$, and 460); 3D $\phi_{3D} = 0.40, 0.42, 0.52, 0.52, 0.54, 0.54$, and 0.57. These parameters increase from left to right in each panel; or equivalently, from bottom to top.

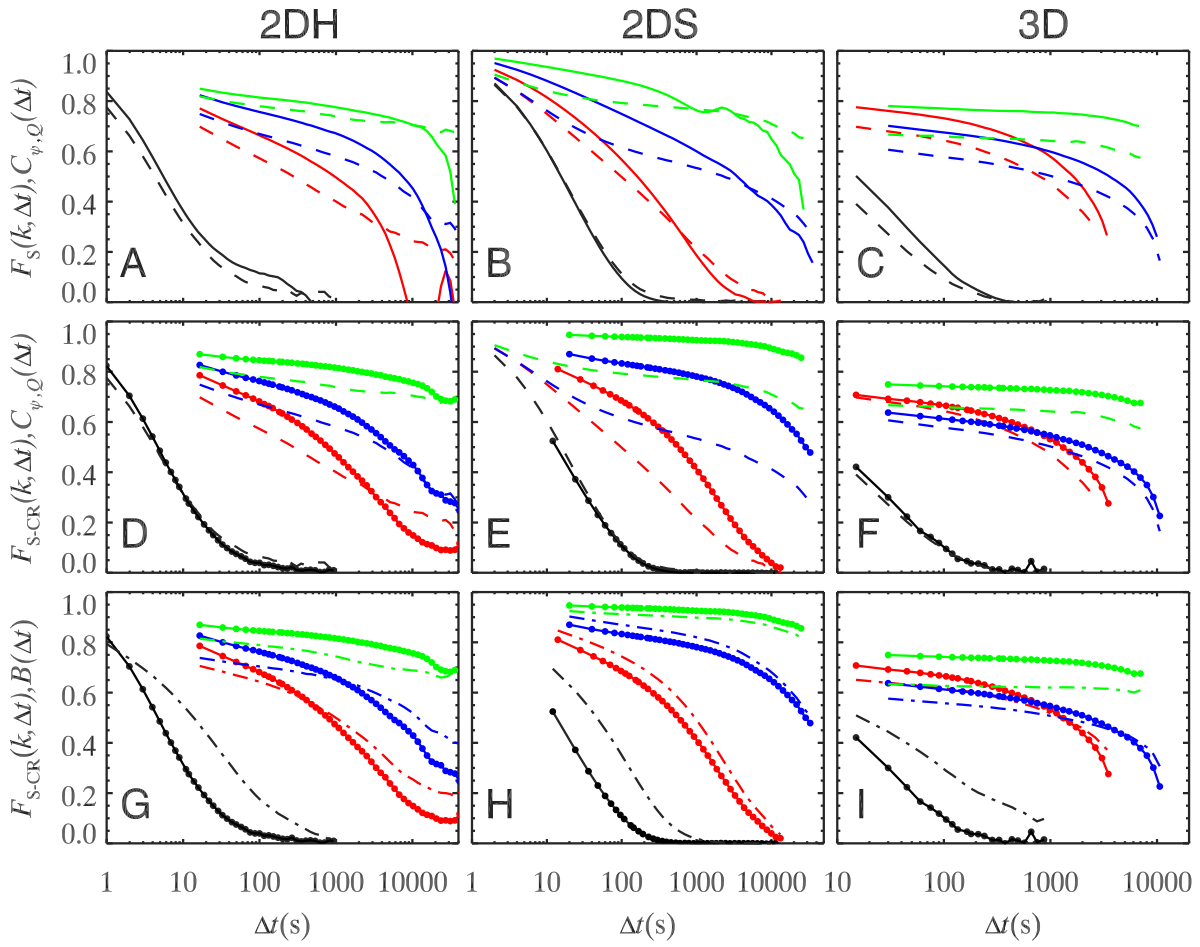

Figure 3.4: Translational, bond-orientational, and bond-break correlation functions. (*A-C*) The solid curves are $F_S(\Delta t)$ (translational correlations) and the dashed curves are $C(\Delta t)$ (bond-orientational correlations) for the 2DH, 2DS, and 3D samples as labeled. The colors indicate different control parameters. For 2DH the colors black, red, blue, and green denote $\phi_{2DH} = 0.55, 0.75, 0.78$, and 0.78 respectively. For 2DS the colors black, red, blue, and green denote $\Gamma_{2DS} = 60, 180, 310$, and 460 respectively. For 3D the colors black, red, blue and green denote $\phi_{3D} = 0.42, 0.52, 0.54$, and 0.58 respectively. (*D-F*) The solid curves with circles are $F_{S-CR}(\Delta t)$ (cage relative translational correlations). The dashed curves are $C(\Delta t)$ which are identical to those shown in (*A-C*). (*G-I*) The solid curves with circles are $F_{S-CR}(\Delta t)$ (cage relative translational correlations) and the dot-dashed curves are $B(\Delta t)$ (bond-break correlations) for the 2DH, 2DS, and 3D samples.

traditional relaxation time scale τ_α is defined from $F_S(\tau_\alpha) = 1/e = 0.37$. For the bond-orientational correlation functions, we quantify local arrangements of particles through ψ_6 in 2D and Q_6 in 3D, both of which are sensitive to hexagonal order [87]. Decay of the autocorrelation functions for these quantities (Fig. 3.3$D-F$) reflects how particles move relative to one another, thus changing their local structure, whereas decay of F_S reflects motion relative to each particle's initial position.

Specifically, Flenner and Szamel found that $F_S(\Delta t)$ and $C(\Delta t)$ had qualitatively different decay forms in 2D, but were similar in 3D [33]. In particular, $F_S(\Delta t)$ decayed significantly faster than $C(\Delta t)$ for 2D simulations. This means that in 2D particles could move significant distances (of order their interparticle spacing) but did so in parallel with their neighbors, so that their positions were changed but not their local structure.

To compare translational and bond orientational correlation functions of our data, we replot some of the data in Fig. 3.4$A-C$. The translational correlation functions for different parameters are solid curves with different colors. The bond-orientational correlation functions are dashed curves, with same color as corresponding translational correlation functions.

The 2D data of Fig. 3.4$A-B$ exhibit decoupling, whereas the 3D data of C are coupled. For the latter case, coupling means that the two functions decrease together, and their relative positions do not change dramatically as the glass transition is approached. Even for the most concentrated case, for which we do not observe a final decay of either function, it still appears that the two correlation functions are related and starting an initial decay around the same time scale. In contrast, for both 2D cases (Fig. 3.4A, B), $F_{\rm S}$ and C_ψ change in relation to one another as the glass transition is approached. For 2DH (panel A), at the most liquid-like concentration (black curves), C decays faster than F_S (dashed curve as compared to the solid curve). As the glass transition is approached,

initially C decays faster, but then the decay of F_S overtakes C. A similar trend is seen for 2DS (panel B). For both 2DH and 2DS, the decoupling is most strongly seen for the most concentrated samples (green curves), for which $F_{\rm S}(\Delta t)$ decays on experimental time scales but where $C_\psi(\Delta t)$ decays little on the same time scales.

The slower decay of bond-orientational correlations relative to translational correlations for our 2D data is in good qualitative agreement with Flenner and Szamel's observations [33]. The meaning is that on approaching the glass transition in 2D, particles are constrained to move with their neighbors such that C decays less than might be expected, on time scales where F_S has decayed significantly. In 3D, however, on approaching the glass transition apparently particles move in a less correlated fashion. To quantify the correlated motion of neighboring particles we compute a two-particle correlation function [32, 88]. This function correlates the vector displacements of pairs of nearest neighbor particles (see Methods). In Fig. 3.5, we show these correlations: 1 corresponds to complete correlation, and 0 is completely uncorrelated. For both 2D samples (solid symbols) the correlations increase for larger τ_α, as indicated by the fit lines. This increased correlation reflects particles moving in parallel directions with their nearest neighbors. For the 3D data (open squares in Fig. 3.5) the correlations are small and do not grow as the glass transition is approached. Particle motion uncorrelated with neighboring particles will decorrelate both positional information and bond-orientational structure.

To qualitatively visualize the differences between dynamics in 2D and 3D, the top row of Fig. 3.6 shows displacement vectors for particles in the three samples near their glass transitions. For both 2DH and 2DS samples, there are clusters of particles moving in similar directions as seen by adjacent displacement arrows pointing in a similar direction. This clustering is less pronounced in 3D, consistent with the small correlations between nearest neighbor motions in 3D (Fig. 3.5).

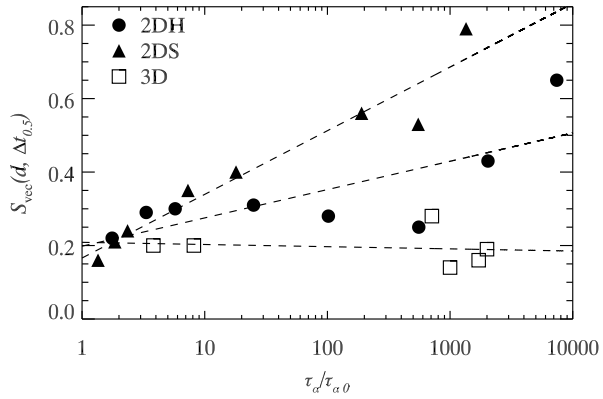

Figure 3.5: Vector displacement correlations. The data are for 2DH (filled circles), 2DS (filled triangles), and 3D (open squares). The displacements are calculated using a time scale Δt such that $F_S(\Delta t) = 0.5$. These are measured for all pairs of particles separated by the nearest neighbor spacing d. d is determined from the large-large peak position in the pair correlation function $g(r)$ at the highest concentrations, and has values $d = 3.38, 6.5$, and 3.10 μm for 2DH, 2DS, and 3D respectively. (The location of the $g(r)$ peak depends slightly on ϕ for 2DH and 3D experiments, and more strongly on Γ for the 2DS experiments; for consistency, we keep d fixed to these specific values.) The lines are least-squares fits to the data. The data are plotted as a function of $\tau_\alpha/\tau_{\alpha 0}$ where $\tau_{\alpha 0}$ is the relaxation time scale for the large particles in a dilute sample. 2DH (closed circles), 2DS (closed triangles), and 3D (open squares) samples have $\tau_{\alpha 0} = 5.4$, 20, and 3.8 s respectively.

As suggested in the Introduction (Sec. 3.1), it is plausible that some of the significant translational motion in the 2D samples is due to Mermin-Wagner fluctuations which act at long wavelengths [35, 83]. To disentangle the potential influences of long wavelength fluctuations from relative motions, we subtract collective motions by measuring "cage relative" particle motions [84]. The key idea is to measure displacements relative to the average displacements of each particle's nearest neighbors, that is, relative to the cage of neighbors surrounding each particle. Previous work has shown that using cage-relative coordinates reveals the dynamical signatures of phase transitions for systems of monodisperse colloids [77]. We compute these cage-relative displacements and then calculate the self-intermediate scattering function $F_{\mathrm{S-CR}}$ using these new displacements.

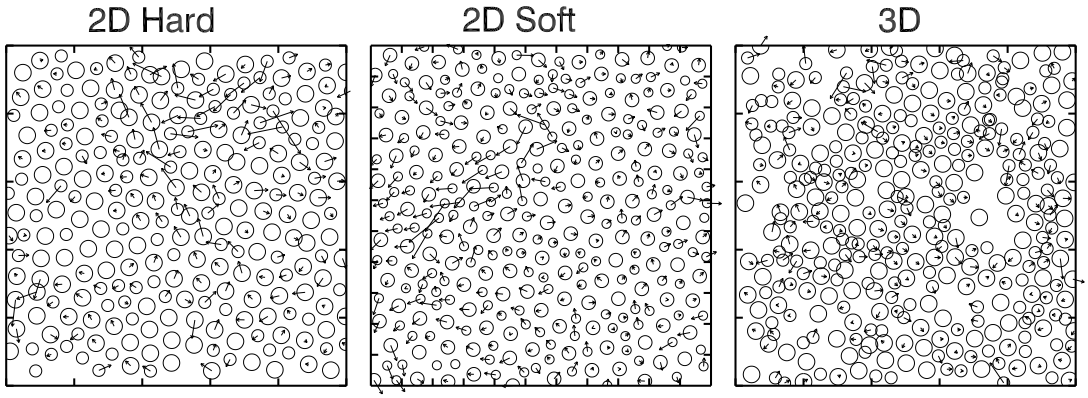

Figure 3.6: Particle displacements. These images show displacement vectors of particles using a time interval Δt chosen such that $F_s(\Delta t) = 0.5$. For the 3D image we use an xy cut at fixed z. All scale ticks are at 10 μm intervals and all displacement vectors are multiplied by two for easier visualization. The circles denote particle positions and sizes. Samples are $\phi_{2DH} = 0.78$, $\Gamma_{2DS} = 300$, and $\phi_{3D} = 0.54$, from left to right, with corresponding $\Delta t = 4290, 1720$, and 3540 s. τ_α for these samples are 10000, 3800, and 7600 s respectively. Circles with no arrows are those with displacements less than 10 % of symbol size.

These are plotted as solid lines with circles in Fig. 3.4$D - F$, with the dashed lines being the bond-orientational data (which are unchanged as $C(\Delta t)$ is always calculated relative to neighbors). In both 2DH and 2DS, $F_{S-CR}(\Delta t) > F_S(\Delta t)$ (the solid lines in Fig. 3.4D, E are higher than the corresponding solid lines in Fig. 3.4A, B). This is expected given the arguments above, that particles move with their neighbors, hence subtracting nearest neighbor motions results in reduction of particle mobility. For the 3D data (Fig. 3.4F), the $F_{\mathrm{S-CR}}(\Delta t)$ curves still show coupling to $C_{\mathrm{Q}}(\Delta t)$ similar to the original data shown in A.

To provide a complementary view, we consider another measure of structural changes, the cage correlation function (or bond-breaking function) $B(\Delta t)$. $B(\Delta t)$ is the fraction of particles that have the same neighbors at times t and $t + \Delta t$, averaged over all initial times t [89, 94].

These functions are plotted in Fig. 3.4$G-I$ as dash-dotted lines, and are compared to $F_{\mathrm{S-CR}}$. The black curves are the lowest concentrations, which all have $B(\Delta t) > F_{S-CR}(\Delta t)$. This is because at lower concentrations, particles can translate a significant amount without losing neighbors. However at larger concentrations, $B(\Delta t) \sim F_{S-CR}(k, \Delta t)$ in all 3 types of samples. For all three experiments, the two correlation functions look fairly similar at the three highest concentrations shown in Fig. 3.4$G-I$. In particular, the differences between the 2D and 3D data are much reduced as compared with the original analysis shown in panels $A-C$.

In fact, our strongest qualitative evidence for coupling comes from comparison of the green curves in Fig. 3.4, which are the samples closest to the glass transition. In each case, the correlation functions do not fully decay within our experimental observation time. Nonetheless, it is apparent for the 2D data that the normal self-intermediate scattering function is beginning a final decay at a time scale for which the bond-orientational function has not yet begun to decay (Fig. 3.4A, B). This is not the case for the 3D data (panel C). In contrast, all three data sets exhibit similar behavior at the largest time scales when comparing the cage-relative $F_{S-CR}(k, \Delta t)$ and $B(\Delta t)$ (panels $G-I$).

We turn now to the question of transient localization, which Flenner and Szamel found to be present in 3D but not 2D. The trajectories of 3D particles showed localized motions separated by abrupt jumps, while trajectories of 2D particles did not have these two distinct types of motion [33]. In their data, this caused a plateau in the 3D MSD, which was not seen in the 2D MSD. The idea is that particles are trapped in cages formed by their neighbors, so for a range of time scales Δt, their MSD should be set by the cage size – assuming particles are localized [89].

Motivated by the considerations above, we investigate the cage-relative mean square displacements (CR-MSD) [84]. Figure 3.7 shows the original MSD data (thin lines) and

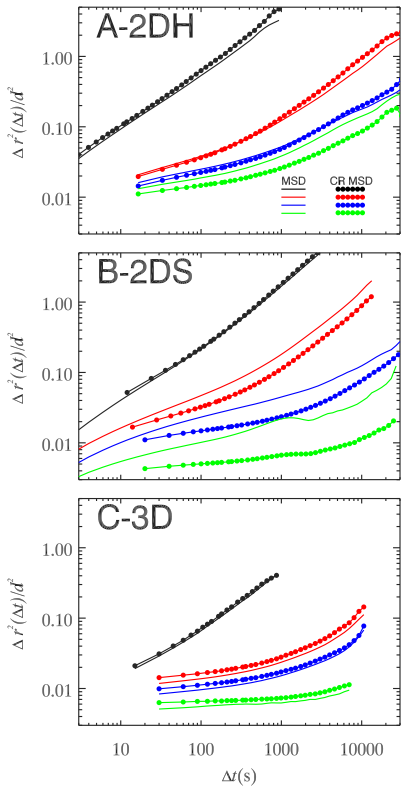

Figure 3.7: Mean square displacements and cage-relative mean square displacements. The data $(A-C)$ are for the experiments as indicated. The solid curves are mean square displacements $< \Delta r^2 >$ calculated for all particles, normalized by d as described in the caption to Fig. 3.5. The solid curves with circles are cage relative mean square displacements. The colors indicate different control parameters, as given in Fig. 3.4. For the 3D samples, the z direction is neglected due to noise and also to facilitate the comparison with the 2D experiments.

CR-MSD (lines with circles). For all experiments, as the concentration increases, the MSD takes a longer time Δt to reach the same point on the vertical axis, reflecting the slowing dynamics on approaching the glass transition. In some cases, the CR-MSD is larger than the MSD (for example, all the curves in Fig. 3.7C). In these situations, the motion of each particle is less correlated with the motion of its neighbors, so the cage relative analysis effectively adds a random vector to each particle's displacement,

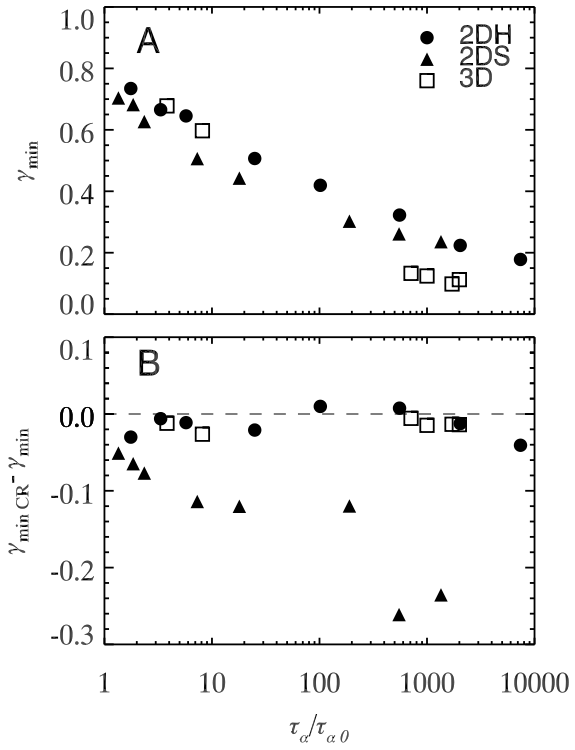

Figure 3.8: Transient localization parameter. (A) $\gamma_{\mathrm{min,CR}}$ is the minimum logarithmic slope of the cage-relative mean square displacements. (B) Difference $\gamma_{\mathrm{min,CR}} - \gamma_{\mathrm{min}}$ between the original mean square displacement data and the cage-relative version. Negative values indicate the enhancement of measured transient localization using the cage-relative analysis.

thus increasing the MSD on average. However, for the 2D samples as they approach the glass transition, the opposite occurs. Especially for the green curves in Fig. 3.7A, B, the data closest to the glass transition, it is clear that the cage-relative analysis dramatically decreases the CR-MSD data relative to the original MSD.

To quantify transient localization, we measure the instantaneous logarithmic MSD slope γ from $\langle \Delta r^2 \rangle = \Delta t^{\gamma(\Delta t)}$. $\gamma = 1$ corresponds to normal diffusion. We quantify the amount of localization by the minimum value of this slope, γ_{min}; this is the logarithmic slope at the inflection point of the MSD or CR-MSD. Figure 3.8A shows the CR data

for the 2D samples (filled symbols) and 3D (open squares) as a function of τ_α. While the 3D data reach lower values, the overall trend is similar between 2D and 3D: the closer to the glass transition, the more pronounced transient localization is. Note that in the work of Flenner and Szamel, they tested both Newtonian dynamics and Brownian dynamics; the latter is more appropriate for colloids. With Brownian dynamics in 2D, they found slightly more pronounced MSD plateaus. It is possible that the presence of Brownian dynamics in our experiments also contributes to our observed similarities in transient localization between 2D and 3D.

Figure 3.8*B* shows the slight enhancement of transient localization caused by the cage relative analysis. We plot the change in $\gamma_{\min}$ upon using the cage relative analysis, and it is generally negative. The largest changes are seen in the 2DS data (solid triangles), which is sensible as these are the data with the strongest correlations with their neighbors.

3.4 Simulations

Flenner and Szamel [33] observed fundamental differences in 2D and 3D simulations approaching the glass transition, that we have explained through our experiments. In this section we show that the analysis used on our experiments reveals the same qualitative results in simulations.

Flenner and Szamel's simulations were done in bidisperse systems with Lennard-Jones(LJ) potential. Here we do simulations in similar systems. For 3D, we use a 80:20 binary Lennard-Jones system, introduced by Kob-Anderson [86]. For 2D we use a 65:35 variant to avoid crystallization [33, 91]. See Sec. 3.2 for more details. Flenner and Szamel saw that in 2D simulation size affected dynamics, not in 3D. They also saw that larger the system size, more the difference in 2D and 3D.

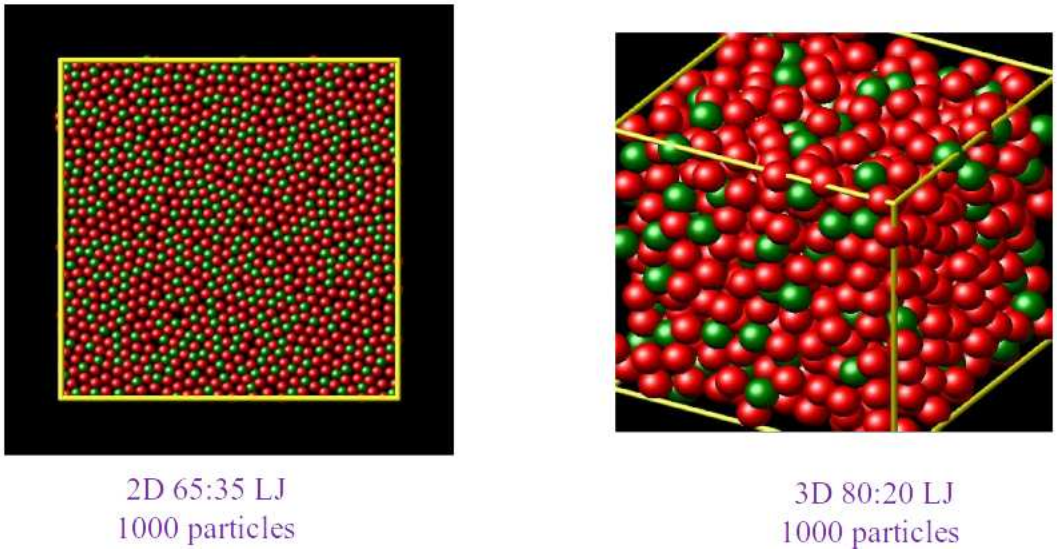

Figure 3.9: 2D and 3D representative Lennard-Jones simulations. Simulations were performed using the LAMMPS package.

Here, we simulate 10000 particles in 2D to see the effects seen by Flenner and Szamel, while 1000 particles in 3D - exactly the same as the canonical system introduced by Kob and Anderson [86]. For 10000 particles, we begin to see the effects seen by Flenner and Szamel, though not as obvious, as they used 4 million particles. However, in simulations temperature T is the control parameter. Decrease in T is analogous to increasing concentration ϕ of the experiments.

In Fig. 3.10a,b we see translational and bond-orientational functions for both 2D and 3D samples at different temperatures. This is analogous to the experimental Fig. 3.4. In Fig. 3.10a, we see that bond-orientational and translation functions show similar behavior for the black curves. But as T decreases, we see the bond-orientations have a slower decay than the translations, thus decoupling occurs in 2D simulations. However for 3D in Fig. 3.10a, we see that both translations and bond-orientations have similar decay, and the former is always larger, even at the lowest temperatures.

Next we measure cage relative translations(F_{S-CR}) shown by the solid line with circles in Fig. 3.10c,d. We use the same measure as in the experiments (see Sec. 3.2) - basically translations after subtracting out any long wavelength fluctuations. Interestingly, we see that for 2D, cage relative translations become much higher than regular translations whereas for the 3D the situation is not changed. This large increase in cage relative translations was also seen in 2DS experiments (Fig. 3.4e). Hence, long wavelength fluctuations are affecting 2D and not 3D simulations.

Next we use the bond-break instead of bond-orientational function, which is a better choice than the latter, same as in experiments(see Sec. 3.2, see Sec. 3.3). In Fig. 3.10e,f we see that 2D and 3D panels now look similar to one another. Thus, differences between 2D and 3D simulations disappear on removing 2D long wavelength fluctuations. We expect our results to hold at even larger 2D system sizes as the only difference would be larger long wavelength fluctuations that will be removed by the analysis.

3.5 Discussion

Our experiments show apparent differences in dynamics approaching the 2D and 3D colloidal glass transition, in agreement with the simulation results of Flenner and Szamel [33].

In 2D, we observe that particles move in parallel with their neighbors, such that their local structure changes less than if the motions were uncorrelated. While it is clear from prior work that in 3D particle motions have some correlation with their neighbors [88], in our data the correlations are more significant for the 2D samples. These are likely related to Mermin-Wagner fluctuations / the Peierls instability in 2D [18, 19, 81–83, 95].

Our 2D samples are, of course, quasi-2D. Both are influenced by nearby large 3D

regions of fluid. The 2DH sample also has hydrodynamic interactions between particles and the nearby bottom of the sample chamber. We find that 2DS samples are more affected by long-wavelength fluctuations than 2DH, which could be due to the difference in interactions [82, 96]. It is certainly plausible that softer interactions allow for more fluctuations in the nearest-neighbor distance, whereas for dense samples with hard interactions, fluctuations are by necessity smaller (as particles cannot move too close together before they repel) [83]. Recent simulation work has shown differences in correlation lengths for disks with soft and hard interaction potentials during 2D melting [97]. Nonetheless, the agreement between the two 2D data sets is striking, especially given the different particle interaction potentials. Namely as distinct from the 3D samples, both 2D samples show large Mermin-Wagner fluctuations.

Another important experimental factor is the system size: approximately $10^5 - 10^6$ particles for both 2D systems and 10^9 for the 3D system. It is likely that for even larger 2D systems, the Mermin-Wagner fluctuations would be more pronounced [33, 35, 98].

Klix, Maret, and Keim [95] recently argued that Mermin-Wagner fluctuations should be present in glassy systems. Probably the most interesting aspect of our study is the suggestion that indeed 2D Mermin-Wagner fluctuations are present in our amorphous samples. Mermin-Wagner fluctuations conventionally result from elasticity associated with the development of an order parameter. The origin of elasticity in glassy systems is less well understood.

Even though our experiments are quasi-2D, we should still observe Mermin-Wagner fluctuations. Slight out of plane fluctuations do not affect how particles are oriented with their neighbors, that cause long-wavelength fluctuations. Also the 2DS system lies on a fluid-fluid interface, and the surface may have slight undulations.

However, the idea is that the topology in 2D causes thermal fluctuations to add up as

long-wavelength fluctuations. This should not be affected by slight out of plane motions or slightly undulating surfaces.

While we have not proven that our observed long-wavelength fluctuations are indeed Mermin-Wagner fluctuations, one could vary the system size in future investigations to examine how the difference between conventional and cage-relative measurements depends on system size. In conclusion, with our efforts and other recent work, there is a compelling collection of evidence that 2D and 3D glass transitions are fundamentally the same: there is strong qualitative agreement between our observations studying three colloidal systems, our simulations, the colloidal experiments and simulations of Illing *et al.* [83], and the soft particle simulations of Shiba *et al.* [35].

The similarities between the conclusions, despite the differences in methods and dynamics, suggest the results are independent of the details. All of these observations show that the 2D glass transition is similar to the 3D glass transition, but with the added influence of Mermin-Wagner fluctuations in 2D.

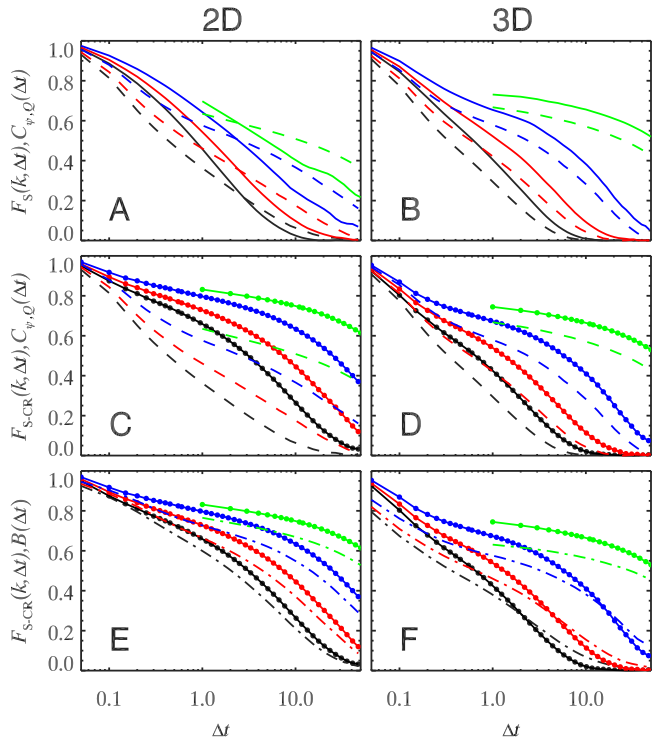

Figure 3.10: Translational, bond-orientational, and bond-break correlation functions. (*A*-*B*) The solid curves are $F_S(\Delta t)$ (translational correlations) and the dashed curves are $C(\Delta t)$ (bond-orientational correlations) for the 2D and 3D simulations. The colors indicate different control parameters. The colors black, red, blue, and green denote $T = 1.0, 0.8, 0.6$, and 0.5 respectively. (*C*-*D*) The solid curves with circles are $F_{S-CR}(\Delta t)$ (cage relative translational correlations). The dashed curves are $C(\Delta t)$ which are identical to those shown in (*A*-*B*). (*E*-*F*) The solid curves with circles are $F_{S-CR}(\Delta t)$ (cage relative translational correlations) and the dot-dashed curves are $B(\Delta t)$ (bond-break correlations).

Chapter 4

Shape dependence approaching the 2D colloidal glass transition

4.1 Introduction

A comprehensive explanation for the dramatic increase in viscosity on approaching the glass transition is still lacking, although there are a variety of theories [25–27]. What makes the matter more complicated is the inadequacy of the traditional concept of viscosity and its relation with microscopic diffusion in supercooled liquids. In liquids, the Stokes-Einstein-Sutherland equation [9, 10] relates microscopic translational diffusion (D_T) as inversely proportional to solvent viscosity η, shown in Eqn. 4.1, where a is particle radius and T is temperature.

$$D_T = \frac{k_B T}{6\pi\eta a}, \tag{4.1}$$

For spherical particles, rotational diffusion follows Eqn. 4.2. This is known as the

Stokes-Einstein-Debye relation and was originally found by Debye [41].

$$D_R = \frac{k_B T}{8\pi\eta a^3}, \tag{4.2}$$

In simple liquids, both viscosity and diffusion are linked to a single timescale of structural relaxation. Further, the ratio of translational to rotational diffusion constants (D_T/D_R) should be independent of viscosity and temperature. However, many experiments and simulations [42–45] have shown a violation of the Stokes-Einstein and Stokes-Einstein-Debye relations in supercooled liquids. Pioneering experiments observed a violation of these relations on approaching the glass transition in a molecular glass former, orthoterphenyl (OTP) [42, 43]. The traditional method to determine diffusion coefficients is through mean square displacements:

$$\langle \Delta r^2(\Delta t) \rangle = 4 D_T \Delta t \tag{4.3}$$

Rotational diffusion coefficient (D_R) is measured from mean rotational MSD as:

$$\langle \Delta\theta^2(\Delta t) \rangle = 2 D_R \Delta t \tag{4.4}$$

where $\Delta\theta$ is the angular displacement in time Δt.

However, the OTP experiments indirectly measured translational and rotational diffusion constants through spin-relaxations, as it was not possible to directly image molecule motions. They used protonated OTP (OTP-h) for measuring D_T and perdeuterated OTP (OTP-d) to measure D_R. They found that $D_{T,R} \sim \eta^{-\xi}$, where $\xi = 0.75$ for translation, and 1 for rotation. Thus they observed an enhancement of translation relative to rotation approaching the glass transition. Later experiments in molecular glasses found different

ξ, ranging from 0.73 to 0.8 [24, 46].

At the time, this strange difference was attributed to spatial distribution of rotational timescales $\rho(\tau)$, and measured rotation and translation measurements being sensitive to different moments of this distribution [24]. To give a better idea, measurements of D_T corresponded roughly to Eqn. 4.3. Corresponding to rotations, the experimental measurements corresponded to the Debye formalism [41, 43, 99]:

$$\tau_c = \int_0^\infty \langle P_2(0)P_2(t)\rangle dt \tag{4.5}$$

$$D_r = 1/6 < \tau_c > \tag{4.6}$$

where $P_2(t) = \frac{3}{2}cos^2(\phi(t)) - \frac{1}{2}$ denotes the second order Legendre polynomial, and $\phi(t)$ is the angle made by the C-H bond vector of the OTP-d molecule with the external magnetic field. $D_R \sim < \tau_c >^{-1}$, whereas $D_T \sim < \tau_c^{-1} >$. In the picture that both rotation and translation are connected to the same timescales $\tau \sim \tau_c$, it was thus concluded that decoupling occurs due to measurements being sensitive to different moments of τ [24].

Advancements in simulation and colloidal techniques has made it possible to directly measure rotational and translational diffusivities at the single particle level [37, 39, 100, 101]. Interestingly in a simulation of a supercooled liquid of dumbbells, it was found that translation-rotation decoupling occurs at the single particle level. They used essentially the same method to determine both D_T and D_R through mean square displacements(Eqns. 4.3,4.4). They observed an enhancement of rotation relative to translation, opposite to previous experiments in OTP. However, when they measured $< \tau_c >^{-1}$ from the Debye method similar to OTP experiments, translation was slightly enhanced relative to rotation.

Hence while they did observe that different measurements of D_R gave differing results, they also observed that even on using the same method for rotation and translation, there was still decoupling. Thus the previous hypothesis that decoupling occurs purely due to difference in measurement methods was ruled out.

The current hypothesis is that decoupling occurs due to translation and rotation degrees encountering different dynamic length scales [102]. Thus, the "single time picture" fails in supercooled liquids [102]. This failure of the "single time picture" can now be understood as a consequence of spatial heterogeneity of dynamics [44, 102–104]. For translation, the picture is better understood. Simulations [44, 104] observed that on measuring structural relaxation time τ_α at wavelengths longer than a characteristic length scale, D_T and τ_α remain coupled. Thus the product $D_T\tau_\alpha$ was completely determined by the length scale of spatially heterogeneous dynamics.

However the difference between rotation and translation and hence the relation of D_T/D_R to spatial heterogeneity of dynamics is unclear. In fact, a number of experiments and simulations yield different results on the nature of decoupling [39, 42, 47]. One key feature to be noted is that all these simulations have different shaped particles. Recent experiments on ellipsoidal glasses [36] found that longer ellipsoids formed liquid crystal phases, while shorter aspect ratio ellipsoids formed glass-like phases.

Recent experimental advances in the field of single-molecule spectroscopy have now made it possible to image actual rotation of fluorescent probes [105–107]. A concern is over what features an 'ideal probe' should posses. Recent simulations found that probe size and roughness greatly influences its dynamics [108, 109]. In fact unlike in simple liquids, probes can largely influence results. In one study [110], rhodamine 6G embedded in o-terphenyl showed indications that the probes experienced different dynamics in the probe. One recent study used the probe BODIPY268, similar in size and mobility to

the host o-terphenyl [107]. They suggested the seemingly obvious, that the ideal probe resembles the host as far as possible. In fact this 'ideal probe' was the key feature that distinguished their work from previous experiments. However, these experiments and most other experiments measure rotation and connect rotation to spatial heterogeneity. Translation is harder to measure, as monitoring translations of typical single molecule probes is likely to require sub-diffraction localization [107].

Colloidal samples at high concentration have been established as model glass formers [28–31], and have the advantage that individual particles can be visualized. One experiment showed an enhancement of rotation relative to translation in spherical colloids [48] approaching the glass transition. In this 'hydrodynamic regime', particle rotation is not hindered as much as translation, in a concentrated suspension. This is because as concentration increases, particles find it harder and harder to translate large distances. In order to do so, they need to break out of a cage of surrounding neighbors (Fig. 4.1). However, rotation is less affected as spheres do not need to interact with their neighbors to rotate in position (Fig. 4.1).

In another colloidal experiment of tetrahedral tracers in a spherical bath, the opposite was seen. In this regime translation was enhanced relative to rotation on approaching the glass transition [37]. This is the 'steric regime,' where rotation is more sterically constrained than translation. Interestingly they observed $D_T \sim \xi^{-0.73}$, and $D_R \sim \xi^{-1}$. The exponents are very close to those measured in OTP.

Thus, probe properties play a significant role in translation-rotation decoupling. An unaddressed question is the influence of probe shape on translation-rotation decoupling. Here using colloidal suspensions, we show that probe shape plays a big role in decoupling.

In this study, we observe naturally occurring silica dimers embedded in a 2D bidisperse glass of silica colloids. These dimers are at a very low concentration, less than 10 percent

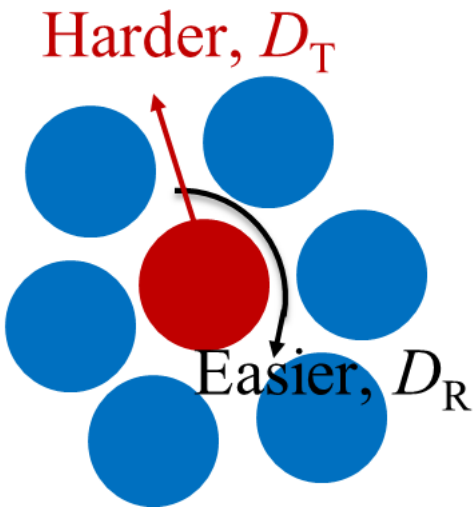

Figure 4.1: Cartoon of rotation v/s translation for a spherical colloidal glass. Red particle finds it harder to break out of cage of neighboring blue particles at large concentration, hence translation is harder. Whereas rotation becomes decoupled, as particle can rotate without cage breaking and hence rotation is easier.

and the experiments are the same as in Chapter. 3. We find that for dimers of smaller lengths, rotations do not slow down as much as translations, on approaching the glass transition, similar to the case of spheres as probes [48]. However we find that in our longest dimers, D_T and D_R remain coupled at all concentrations, i.e. $D_T/D_R \sim$ constant. Hence in our samples, long dimers are 'ideal probes' in terms of rotation reflecting translation.

We must be careful in interpreting our results in the context of real glass formers. Our experiments are in the 'hydrodynamic regime,' which is only present in colloidal systems. Also, our particles have hard interactions, different from real glass formers. To see if this regime is present in other glass formers, we do Lennard-Jones simulations, similar to Sec. 3.4, but add a tracer dimer of chosen length, as observed in our experiments. Interestingly, we observe similarities between experiments and simulations in decoupling between D_T and D_R, based on dimer length. However in the simulation liquid regime,

short dimers have D_R greater than large dimers by more than an order of magnitude. Whereas in the colloidal experiments at lowest concentration, the difference between D_R of long and short dimers is less than a factor of 2.

4.2 Imaging and tracking dimers

Thus far, the code in the Weeks lab has been mainly for tracking circular/spherical objects [63]. For analyzing dimers, I built additional algorithms to recognize the shape of dimers. The first step was to track the two particles of a dimer, as shown in Fig. 4.2b. Then I selected the region of the image (ROI) that included dimers. Based on brightness, I thresholded this ROI to get a bi-level image, with the features of interest in white, and the background as black (Fig. 4.2c). On this bi-level image, I used the `LABEL_REGION` function from IDL to identify blobs, and selected the largest blob as the dimer of interest. To find the perimeter, I used the `FIND_BOUNDARY` function, shown in Fig. 4.2d.

Further, to quantify the shape, I measured the longest axis l_l, and short axis l_s perpendicular to l_l. The aspect ratio then is l_l/l_s.

4.3 Hydrodynamic theory

The dimers we analyze have an aspect ratio $\rho = l_l/l_s < 2$, whereas for perfect dumbbells, $\rho = 2$. But to a good approximation, we can model our dimers as dumbbells of an effective radius. For dumbbells in a liquid the ratio of translational to rotational diffusion coefficients [111] is given as

$$\frac{D_T}{D_R} = \frac{\sigma^2}{4} \tag{4.7}$$

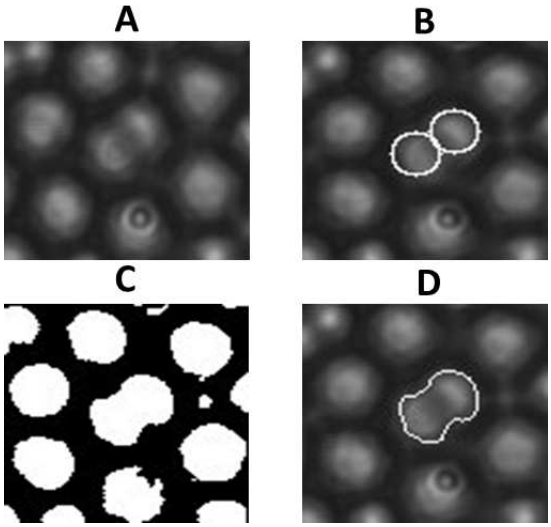

Figure 4.2: (A) Image of a dimer surrounded by spherical particles. (B) Tracking dimers. (C) Thresholding image. (D) Outlining dimers. The aspect ratio of the dimer is 1.65. The size of the image is $\sim 10\mu$m.

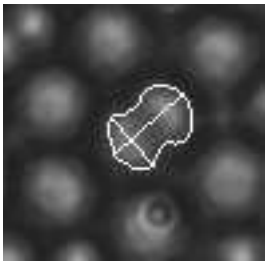

Figure 4.3: Longest axis l_l and perpendicular short axis l_s. The dimer is the same as in Fig. 4.2.

where σ is the diameter of particles in the dumbbell. In our experimental samples at low concentrations (more liquid-like), we can then fit σ to D_T/D_R to calculate an effective diameter σ_{eff} of the two particles in an ideal dumbbell of aspect ratio 2.

4.4 Results

We track the translational and rotational diffusion of dimers [63] in 2D. The sample is the same as 2DH, described in Sec. 3.2. However this sample has some naturally occurring dimers, at less than 5% concentration, which we now analyze. Translational diffusion coefficient(D_T) is measured from mean square displacement(MSD) as in Eqn. 4.3. Rotational diffusion coefficient (D_R) is measured from mean rotational MSD as in Eqn. 4.4.

D_R is easier to measure in 2D compared with previous tracking of colloids in 3D [37, 48], as in 2D there is only one rotational degree of freedom. As the system is bidisperse, there are two kinds of dimers - large-large and small-small. The dimers never dissociate, and the individual particles stay stuck. This implies that the dimers are probably formed in the stock jars before our experiments are begun.

The translational mean square displacement of a dimer is shown in Fig. 4.4, for a slightly supercooled sample. The line drawn is of slope 1 on the log-log axes, indicating diffusive behavior.

At early times, particles show diffusive behavior, when they have not yet bumped into their neighbors. At intermediate times, the sample shows a subdiffusive behavior of log-log slope less than 1, as particles bump into their neighbors and are not free to diffuse about.

At longer times particles have broken out of their ‘cages’ on average, and hence show diffusive behavior. Correspondingly, the fit line at long times is a fit to diffusive behavior,

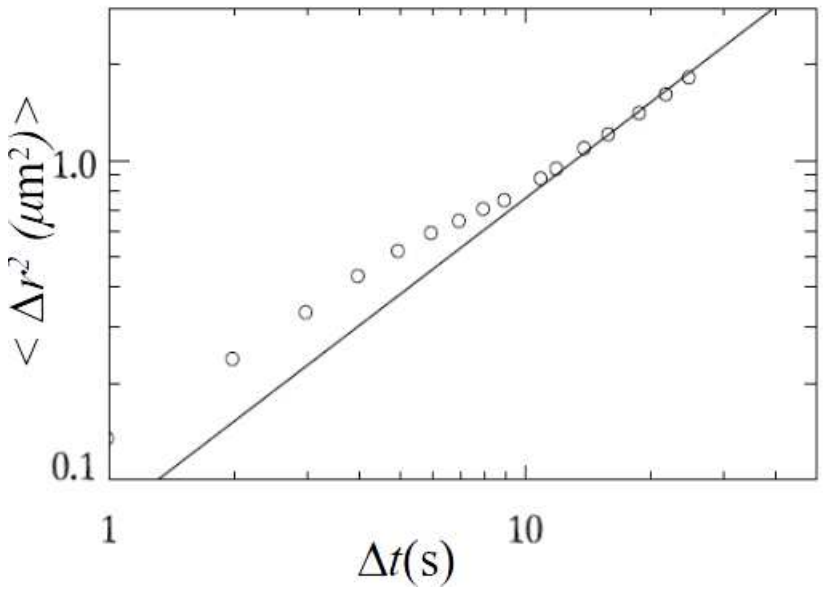

Figure 4.4: Log-log translational MSD of a small-small dimer in a slightly supercooled sample at $\phi = 0.55$. The aspect ratio of the dimer is 1.66. Line is a fit to slope 1. $D_T = 0.019\ \mu\text{m}^2/\text{s}$.

corresponding to Eqn. 4.3. The slope yields D_T. On the log-log plot, the slope is 1, and the intercept is D_T.

Similarly, the rotational mean square displacement is shown in Fig. 4.5, for the same sample. Interestingly, the rotational MSD fits well to slope=1, even at short times. This means that rotation is less affected by supercooling.

To understand how diffusion constants change as a function of supercooling, we plot diffusion constant v/s sample relaxation time τ_α. The measurement of τ_α is described in detail in Sec. 3.3, but the basic idea is to define a correlation function F_S corresponding to translation, and measure the time when $F_S = 1/e$.

Figure 4.6a plots D_T v/s τ_α for all samples. Here we see that all dimers follow the black line of the bulk D_T of the entire sample. The black curve follows $D_T \sim \tau_\alpha^{-0.73}$, in the range of exponents observed in other experiments [37, 43]. Although, viscosity was

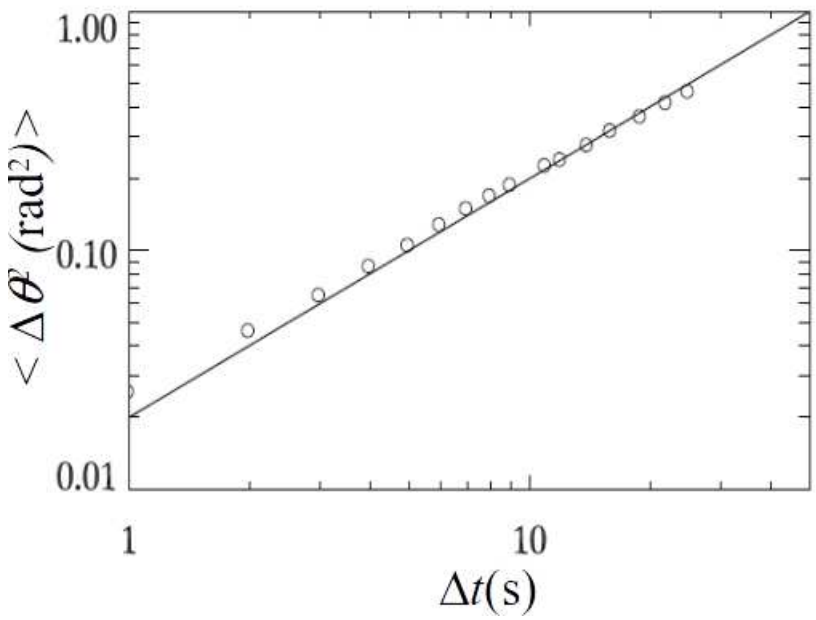

Figure 4.5: Log-log rotational MSD of a small-small dimer in a slightly supercooled sample at $\phi = 0.55$. Line is a fit to slope 1. The aspect ratio of the dimer is 1.66. $D_R = 0.01$ rad^2/s.

measured from the bulk sample and is strictly not the same as τ_α.

D_R however seems to depend a lot more on dimer length l_l, as shown in Fig. 4.6b. Here as τ_α increases, longer dimers show a decrease in D_R as expected (blue diamonds). However the short dimers (red circles and green squares) show a lack of decrease in D_R indicating a lack of slowdown of rotation. We postulate a similar mechanism to the lack of slowdown of rotation seen in spherical colloids ([48] see Fig. 4.1) i.e. smaller dimers are more free to rotate in place as compared to translate out of the cage made of neighboring particles. The difference between D_R of the long and short dimers is more than an order of magnitude at the largest τ_α.

This difference in slowdown of D_R and not D_T based on dimer length is observed on plotting D_T/D_R shown in Fig. 4.6c. The long dimers (blue diamonds) show a constant

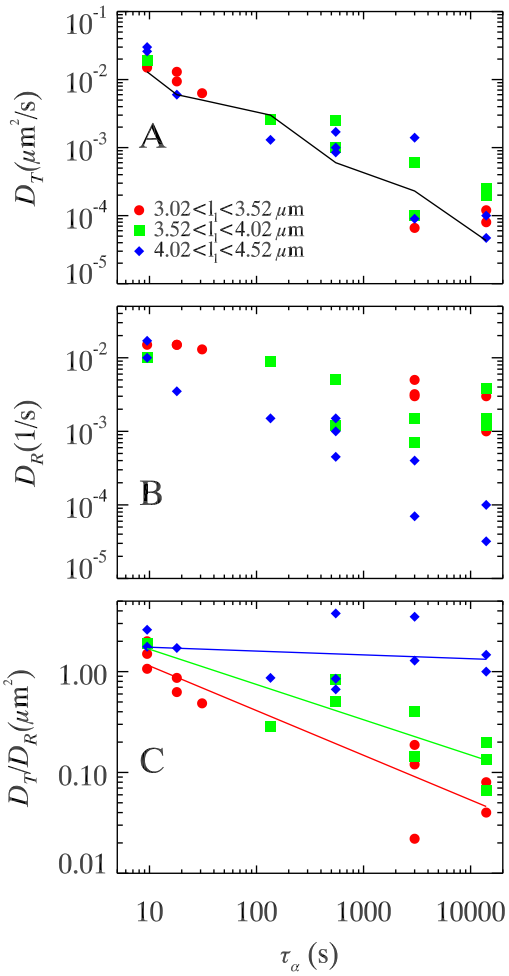

Figure 4.6: Diffusion coefficients vs τ_α for different dimer lengths. (A) D_T v/s τ_α. The line denotes bulk sample D_T. (B) D_R v/s τ_α. (C) D_T/D_R v/s τ_α. Different colors denote different l_l. Red circles, green squares and blue diamonds go from smallest to largest l_l as indicated in the legend.

D_T/D_R independent of τ_α. But the short dimers(red circles) show a decrease in D_T/D_R with τ_α. The colored lines show best fit lines for the three different dimer length regimes. At the largest τ_α, the difference between D_T/D_R of the long and short dimers is more than an order of magnitude.

To understand the dependence of translation and rotation on dimer length, we plot diffusion v/s long axis of dimers in Fig. 4.7. In Fig. 4.7a we see that D_T does not depend on dimer length. But at the lowest τ_α (red circles), D_T is the largest. At higher τ_α, D_T is lower as expected.

However, D_R depends much more on dimer length as can be seen in Fig. 4.7b. Short dimers have similar D_R at all τ_α. And at low τ_α, D_R is almost constant, independent of dimer length. However, at large τ_α, D_R of long dimers differ from short dimers by more than 2 orders of magnitude.

Figure 4.7c shows D_T/D_R vs dimer length. Interestingly, at low τ_α, D_T/D_R seems to be independent of dimer length. In order to see if this makes sense, we compare the semi dilute case at low τ_α with theoretical results for dumbbells [111] diffusing in liquids. For dimers, $D_T/D_R = \sigma_d^2/4$ (see Sec. 4.3). Since our dimers have an aspect ratio < 2, they are not perfect dumbbells in the sense of the theory, which assumes aspect ratio $= 2$. But we can find an effective diameter by fitting D_T/D_R to $\sigma_{eff}^2/4$, at low concentration ($\tau_\alpha = 9.5s$) as

$$\sigma_{eff} = 2\sqrt{\frac{D_T}{D_R}} \tag{4.8}$$

From Eqn. 4.8 we find $\sigma_{eff} = 2.7 \pm 0.4\mu$m. This seems like a good estimate for σ_{eff}, as our two particle diameters. are 2.53 and 3.38 μm. Also the dimers are all aspect ratio < 2, hence we expect σ_{eff} to be less than actual particle diameter. It may seem strange

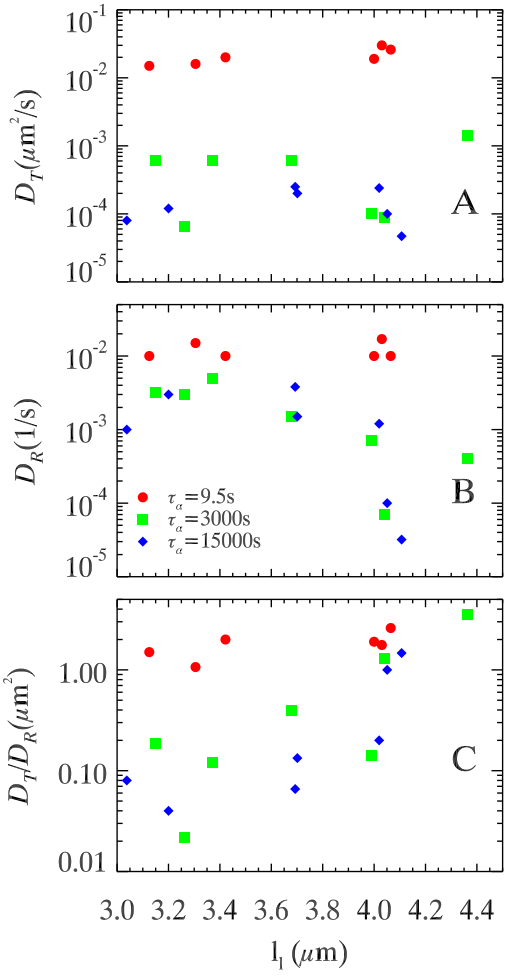

Figure 4.7: Diffusion coefficients vs dimer long-axis length l_l for different τ_α. (A) D_T v/s l_l. (B) D_R v/s l_l. (C) D_T/D_R v/s l_l. Different colors denote different τ_α. Red circles, green squares and blue diamonds go from smallest to largest τ_α as indicated in the legend.

that σ_{eff} is seemingly independent of l_l as there are small-small and large-large dimers. However, on considering the two particle diameters, $2.54, 3.38\mu$m, the ratio between these two σ is 1.33, and hence the ratio of σ^2 is 1.77, which is smaller than the experimental variability of D_T/D_R (~ 2) at low τ_α .

Also our particles may deviate from the dumbbell model, more so at small aspect ratios. At large τ_α, D_T/D_R of long dimers differ from short dimers by around 2 orders of magnitude, reflecting the dependence of D_R on dimer length.

Instead of dimer length, another related variable is aspect ratio. Figure 4.8 shows D_T/D_R v/s τ_α, equivalent to Fig. 4.6c, but different colors denote aspect ratio instead of dimer length. There is no clear trend, and Fig. 4.6c looks better. Hence the longest axis seems to be the relevant parameter, rather than aspect ratio, or eccentricity. This makes sense in the limit that particles are much smaller than surrounding medium, since then even at a large aspect ratio if particle size $\ll$ surrounding medium, particles do not encounter the cage of surrounding particles. It makes sense then, that the longest axis as compared to cage size controls whether or not particle rotation is sterically hindered by their neighbors on approaching the glass transition.

While we have looked at tracer dimers embedded in a glass of bidisperse spheres, other studies have looked at glass transitions in colloidal glasses composed of anisotropic particles [36, 48]. Figure 4.9 is reinterpreted from previous data, along with the results of our dimers (red) plotted as a function of aspect ratio. All the points shown are equilibrated data at high measured concentration,closest to the glass transition.

A value of 1 indicates that D_T/D_R did not change on approaching the glass transition. Less than 1 indicates that translation slowed down more than rotation, as can be seen for aspect ratio less than ≈ 2. For the large aspect ratio 6, however, the y-axis is larger than 1, indicating that rotation slows down more than translation.

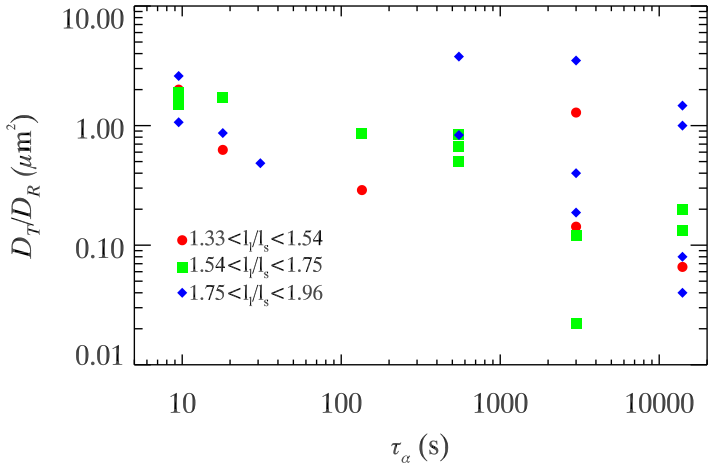

Figure 4.8: D_T/D_R v/s τ_α for different aspect ratio l_l/l_s. Different colors denote different aspect ratio regimes. Red circles, green squares and blue diamonds go from smallest to largest aspect ratios.

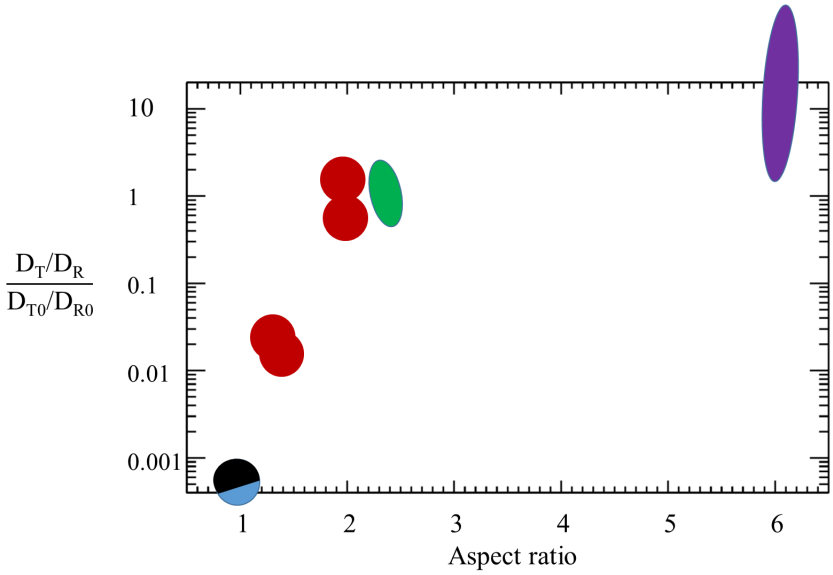

Figure 4.9: D_T/D_R close to the glass transition normalized by dilute value v/s aspect ratio master curve along with previous data. Spheres at low aspect ratio are reinterpreted from [48] (3D experiments). Dimers in red are from the current experiment and span aspect ratio 1.3 to 1.9. Ellipsoids in green and purple denote aspect ratios 2.3 and 6, reinterpreted from [36] (2D experiments).

Although in our experiments, dimer length is more relevant than aspect ratio, our results seem to follow the trend qualitatively. However, this graph should not be interpreted quantitatively due to different experimental procedures. The sphere data come from 3D experiments [48], whereas ellipsoids [36] and dimers are from 2D. Also dimers v/s ellipsoids might decouple differently. Further, rotation and translation is measured differently in different experiments, and we know that different measurement methods might cause slightly different results [24]. Nevertheless, it is very encouraging that all the data fall on the same qualitative master curve.

4.5 Simulations

We did 2D simulations in Lennard-Jones systems, similar to Sec. 3.4 the difference being that we used smaller number of particles (500) and embedded a dimer. The reason we used smaller number of particles was to remove Mermin Wagner fluctuations that become important as system size increases [35].

We used Lennard-Jones potential in systems evolving with Newtonian dynamics in an NVT ensemble. The simulations were performed using LAMMPS [90].

We simulated a 65:35 binary mixture of Lennard-Jones particles [91].

$$V_{\alpha\beta}(r_{ij}) = 4\epsilon_{\alpha\beta}\left[\left(\frac{\sigma_{\alpha\beta}}{r_{ij}}\right)^{12} - \left(\frac{\sigma_{\alpha\beta}}{r_{ij}}\right)^{6}\right] \tag{4.9}$$

where r_{ij} is the distance between particle i and j, and α and β denotes the type of particle. We denote the majority species as the A particles and the minority species as the B particles; the potential parameters are given by $\epsilon_{BB} = 0.5\epsilon_{AA}$, $\epsilon_{AB} = 1.5\epsilon_{AA}$, $\sigma_{BB} = 0.88\sigma_{AA}$, and $\sigma_{AB} = 0.8\sigma_{AA}$. We present results in reduced units, where the unit of

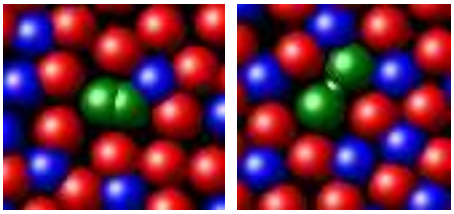

Figure 4.10: Dimer embedded in glass simulation images. Left: Image of a short (green) dimer ($l_l = 1.33\sigma$) surrounded by bath of particles. Right:Image of a long (green) dimer ($l_l = 2.0\sigma$) surrounded by bath of particles. Simulations are Lennard-Jones, done using the LAMMPS simulation package.

length is σ_{AA} , the unit of temperature is k_B/ϵ_{AA} , and the unit of time is $\sqrt{(}m\sigma_{AA}^2/\epsilon_{AA})$. The mass for both species are the same. We simulated N = 500 particles at T = 5.0, 1.0, 0.9, 0.8, 0.7, 0.6, and 0.5. The number density is 1.2, same as in [91].

Dimers are modeled as two particles attached through a harmonic bond of large stiffness so that the particles remain stuck [40]. The two particles in the dimer interact with the surrounding medium as type A particles. Interparticle interactions between discs in a single tracer are described by both harmonic bonding (U^b) and bending (U^a) potentials. Bending potentials of large stiffness are invoked so that the two particles in a dimer do not bend relative to one another. All pairs of neighbor discs are bonded tightly by invoking $U^b = 1000k_BT(r/\sigma - l)$, where r is the distance between a pair of neighbor discs. l is the desired separation between the two particles of the dimer.

By this method, we can control the length of the dimer, and hence nature of translation and rotation seen. We choose two values, $l = 0.33, 1.0\sigma$ and hence long axis of dimer $l_l = 1.33, 2\sigma$ respectively, which matches up with the shortest and longest dimers seen experimentally.

Figure 4.11 is the simulation version of Fig. 4.6. In Fig. 4.11a, we see that D_T of long and short dimers are almost the same. This is similar to experiments, where D_T does not

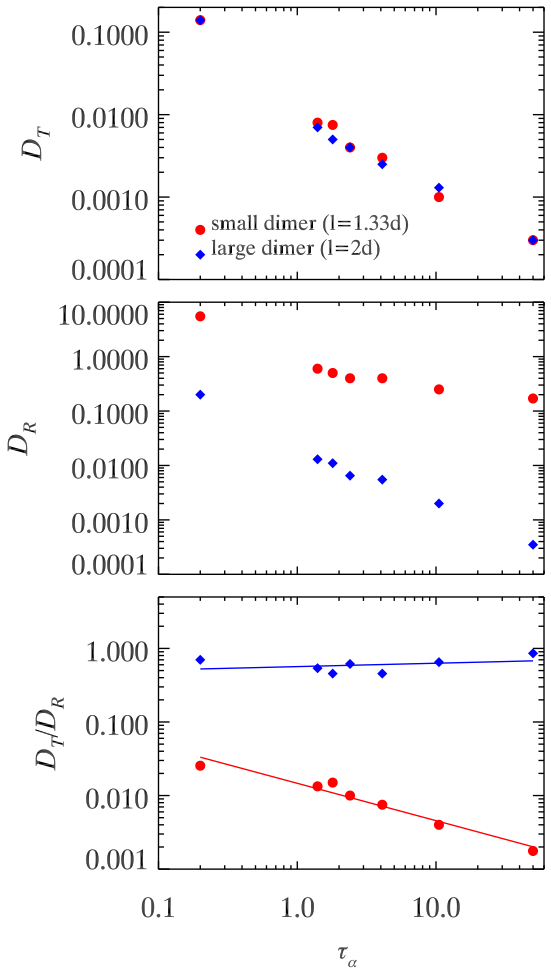

Figure 4.11: Simulation diffusion coefficients vs τ_α for different dimer lengths. (A) D_T v/s τ_α. (B) D_R v/s τ_α. (C) D_T/D_R v/s τ_α. Different colors denote different l_l. Red circles and blue diamonds are $l_l = 1.33, 2.0\sigma$ respectively.

depend on dimer length (Fig. 4.6a). D_R depends on l_l, however, and the short dimers shown in the red circles in Fig. 4.11b show a weaker dependence on τ_α, again similar to Fig. 4.6b. However, interestingly the gap between the red and blue symbols is much larger in simulations, especially obvious at low τ_α. Whereas at small τ_α in experiments, D_R seems independent of τ_α in Fig. 4.6b.

This difference in D_R is reflected in D_T/D_R shown in Fig. 4.11c, whereas in Fig. 4.6c, at low τ_α the red, green, and blue lines seem to have similar intercepts. One reason for this difference between experiments and simulations could be different interaction potentials. Another important difference which may be more relevant, is hydrodynamics, only present in colloidal experiments. At low concentration, colloidal particles translate due to interactions with solvent molecules. Whereas in the simulations, there is no background solvent.

4.6 Conclusions

Remarkably, we see that small changes in dimer length cause huge changes in rotational diffusion. Smaller dimers show a weaker slowdown in rotation on approaching the glass transition. Translation on the contrary is not affected as much. This is in marked contrast to previous experiments in polymer glasses, where translation diffusion was found to be affected by shape, and not rotational diffusion [112]. However, our experiments are in the hydrodynamic regime, where rotation is not as strongly affected by slowing down of dynamics approaching the glass transition, as translation.

In the Lennard-Jones simulations we observed similar results - translational diffusion does not depend on dimer length, but rotational diffusion does, and smaller dimers show a weaker slowdown in rotation on approaching the glass transition. However an important

difference is that at low τ_α in the liquid like regime, simulations show a much larger difference in D_R based on dimer length, than experiments. This is puzzling as the liquid regime is where we would expect simulations and experiments to match. However an important difference is hydrodynamics, only important in colloidal experiments.

Given the large differences in interaction potentials and hydrodynamics, it is remarkable that experiments and simulations yield similar results in the regime where particle rotations show a weaker slowdown approaching the glass transition than translations. It's possible that for larger aspect ratios (trimers, tetramers) we will encounter the steric regime, where rotation slows down more than translation approaching the glass transition. This regime would be more in the realm of polymer experiments that observed translation diffusion was affected by shape rather than rotational diffusion.

Chapter 5

Summary and outlook

During my PhD, I have looked at the influence of dimensionality in materials. This consisted of experiments in two different systems - soap films as model 2D fluids, and 2D colloidal glass formers.

My experimental results reveal that in both of these systems, long-range dynamic correlations arise by virtue of being in 2D. However the importance of other effects such as the influence of the interface varies. Hopefully my results shed light on what aspects of dimensionality are more universal than others. This may pave the way for future studies of dimensionality effects in other types of systems.

5.1 2D liquids and modeling them through soap films

Using tracer particles as probes in soap films, we have probed viscous properties in quasi-2D films. For bulk liquid properties, interfaces are neglected. However in our soap films we find that both interfacial viscosity at the soap-air interface and 3D viscosity of the bulk fluid in the film are important.

We find that while diffusion in thick films acts 3D, flow fields at larger length scales is like a 2D fluid. We develop a new method based on two-particle correlations to measure 2D soap film viscosities.

Further validation and improvement will lie in accurate localization of particles in 2D films, improving errors, and comparing interfacial viscosities in different types of films. Thus for thin films in general, both 2D surface viscosity and 3D bulk viscosity are important.

5.2 2D glass transition

Our results suggest a partial resolution of the question - does dimensionality affect the glass transition? In recent simulations, Flenner and Szamel [33] observed large differences in 2D and 3D glassy dynamics and concluded that the glass transition in 2D is fundamentally different from 3D, contrary to the previous view [30].

Through colloidal glass formers, we demonstrate that the differences between 2D and 3D are precisely those that distinguish 2D and 3D phase transitions. In 2D it has well been known that there are long-wavelength fluctuations (Mermin-Wagner fluctuations [19]). We find that these fluctuations were the reason that 2D and 3D looked different in Flenner and Szamel's simulations. Through a different analysis method that removes the influence of these fluctuations, we show that 2D and 3D glass transitions are otherwise similar.

Understanding properties of low dimensional systems and thin films is important, as well as knowing whether or not dimension plays a role. However, many of these systems are composed of a few layers of atoms, thus different in topology from a single layer. We have argued that the presence of long-wavelength fluctuations are due to 2D topology

and how particles are oriented with respect to their nearest neighbors. Hence, it will be interesting to see if such fluctuations are observed in colloidal systems with a few layers, and if so, to what extent.

5.3 Shape dependent glass transition

It is well known that approaching the glass transition is characterized by a tremendous increase in viscosity [24, 30]. However, due to heterogeneous dynamics, the relation between diffusion and viscosity breaks down, known as the breakdown of the Stokes-Einstein relations [24, 42, 43]. Another related breakdown is the decoupling between translation and rotational diffusion [24, 37, 39, 42, 43], known as the Stokes-Einstein-Debye breakdown.

The origin of of the Stokes-Einstein-Debye breakdown is far from clear. Different measurement methods of diffusivity, different types of glass formers, simulations v/s experiments yield different results [24, 37, 39, 42, 43, 113].

In our experiments, we find that tracer shape largely influences translation-rotation decoupling. In particular, we find that tracer shape largely influences particle rotations. Smaller dimers can rotate much more easily than translate, whereas in our largest dimers, translation and rotation show similar behavior. This is in contrast to previous experiments in molecular glass formers, where shape was found to affect translation rather than rotation [42, 43, 112]. One thing to note is our experimental dimers have smaller aspect ratios than the molecular glass formers. Thus our results are a prediction of diffusive properties in low aspect ratio glasses.

In liquids, the Stokes-Einstein-Debye relations connect microscopic diffusion with macroscopic viscous properties. However in glasses, this relation breaks down. Characterizing this breakdown is an important step in understanding the connection between

the microscopic and macroscopic in glasses. In this regard, colloids are a great system to test the breakdown as a function of particle shape, size, dimension, etc.

More specifically, a valuable extension of the present work would be using colloids to map out the translation-rotation breakdown. Hopefully by using longer particles such as linear trimers, one would see the regime where translation is enhanced relative to rotation, opposite to the current work. This would be a step in understanding the shape dependence of rotational v/s translational heterogeneity and its connection to viscosity and thus getting closer to fully understanding the connection between microscopic and macroscopic properties in glasses.

References

[1] N. D. Mermin, Crystalline order in two dimensions, *Phys. Rev.*, **176**, 250–254 (1968).

[2] H. A. Stone, Interfaces: In fluid mechanics and across disciplines, *J. Fluid Mech.*, **645**, 1–25 (2010).

[3] A. K. Geim and K. S. Novoselov, The rise of graphene, *Nature materials*, **6**, 183–191 (2007).

[4] H. Lamb, *Hydrodynamics* (Cambridge university press) (1932).

[5] M. Doi and S. F. Edwards, *The theory of polymer dynamics*, volume 73 (oxford university press) (1988).

[6] R. Di Leonardo, S. Keen, F. Ianni, J. Leach, M. J. Padgett, and G. Ruocco, Hydrodynamic interactions in two dimensions, *Phys. Rev. E*, **78**, 031406–03146–4 (2008).

[7] H. A. Stone and A. Armand, Hydrodynamics of particles embedded in a flat surfactant layer overlying a subphase of finite depth, *J. Fluid Mech.*, **369**, 151–173 (1998).

[8] J. Crocker, M. T. Valentine, E. R. Weeks, T. Gisler, P. D. Kaplan, A. G. Yodh, and D. A. Weitz, Two-point microrheology of inhomogeneous soft materials, *Phys. Rev. Lett.*, **85**, 888–891 (2000).

[9] A. Einstein, Über die von der molekularkinetischen Theorie der Wärme geforderte Bewegung von in ruhenden Flüssigkeiten suspendierten Teilchen, *Ann. Phys.*, **322**, 549–560 (1905).

[10] W. Sutherland, A dynamical theory of diffusion for non-electrolytes and the molecular mass of albumin, *Phil. Mag. Series 6*, **9**, 781–785 (1905).

[11] P. G. Saffman and M. Delbrück, Brownian motion in biological membranes, *Proc. Nat. Acad. Sci.*, **72**, 3111–3113 (1975).

[12] P. G. Saffman, Brownian motion in thin sheets of viscous fluid, *J. Fluid Mech.*, **73**, 593–602 (1976).

[13] J. R. Samaniuk and J. Vermant, Micro and macrorheology at fluid-fluid interfaces, *Soft Matter*, **10**, 7023–7033 (2014).

[14] B. D. Hughes, B. A. Pailthorpe, and L. R. White, The translational and rotational drag on a cylinder moving in a membrane, *J. Fluid Mech.*, **110**, 349–372 (1981).

[15] E. P. Petrov and P. Schwille, Translational diffusion in lipid membranes beyond the saffman-delbrück approximation, *Biophys. J.*, **94**, L41–L43 (2008).

[16] E. P. Petrov, R. Petrosyan, and P. Schwille, Translational and rotational diffusion of micrometer-sized solid domains in lipid membranes, *Soft Matter*, **8**, 7552–7555 (2012).

[17] Z. H. Nguyen, M. Atkinson, C. S. Park, J. Maclennan, M. Glaser, and N. Clark, Crossover between 2d and 3d fluid dynamics in the diffusion of islands in ultrathin freely suspended smectic films, *Phys. Rev. Lett.*, **105**, 268304–1–268304–4 (2010).

[18] R. Peierls, Bemerkungen über umwandlungstemperaturen, *Helvetica Physica Acta*, **7**, 81–83 (1934).

[19] N. D. Mermin and H. Wagner, Absence of ferromagnetism or antiferromagnetism in one- or Two-Dimensional isotropic heisenberg models, *Phys. Rev. Lett.*, **17**, 1133–1136 (1966).

[20] J. M. Kosterlitz and D. J. Thouless, Ordering, metastability and phase transitions in two-dimensional systems, *Journal of Physics C: Solid State Physics*, **6**, 1181 (1973).

[21] K. J. Strandburg, Two-dimensional melting, *Rev. Mod. Phys.*, **60**, 161–207 (1988).

[22] U. Gasser, C. Eisenmann, G. Maret, and P. Keim, Melting of crystals in two dimensions, *ChemPhysChem*, **11**, 963–970 (2010).

[23] E. P. Bernard and W. Krauth, Two-Step melting in two dimensions: First-Order Liquid-Hexatic transition, *Phys. Rev. Lett.*, **107**, 155704 (2011).

[24] M. D. Ediger, Spatially heterogeneous dynamics in supercooled liquids, *Annual review of physical chemistry*, **51**, 99–128 (2000).

[25] G. Biroli and J. P. Garrahan, Perspective: The glass transition, *J. Chem. Phys.*, **138**, 12A301 (2013).

[26] M. D. Ediger and P. Harrowell, Perspective: Supercooled liquids and glasses, *J. Chem. Phys.*, **137**, 080901 (2012).

[27] A. Cavagna, Supercooled liquids for pedestrians, *Phys. Rep.*, **476**, 51–124 (2009).

[28] W. K. Kegel and A. van Blaaderen, Direct observation of dynamical heterogeneities in colloidal hard-sphere suspensions, *Science*, **287**, 290–293 (2000).

[29] E. R. Weeks, J. C. Crocker, A. C. Levitt, A. Schofield, and D. A. Weitz, Three-dimensional direct imaging of structural relaxation near the colloidal glass transition, *Science*, **287**, 627–631 (2000).

[30] G. L. Hunter and E. R. Weeks, The physics of the colloidal glass transition, *Rep. Prog. Phys.*, **75**, 066501 (2012).

[31] F. Ebert, P. Dillmann, G. Maret, and P. Keim, The experimental realization of a two-dimensional colloidal model system, *Rev. Sci. Inst.*, **80**, 083902 (2009).

[32] B. Doliwa and A. Heuer, Cooperativity and spatial correlations near the glass transition: Computer simulation results for hard spheres and disks, *Phys. Rev. E*, **61**, 6898–6908 (2000).

[33] E. Flenner and G. Szamel, Fundamental differences between glassy dynamics in two and three dimensions, *Nature Comm.*, **6**, 7392 (2015).

[34] S. Sengupta, S. Karmakar, C. Dasgupta, and S. Sastry, Adam-Gibbs relation for glass-forming liquids in two, three, and four dimensions, *Phys. Rev. Lett.*, **109**, 095705 (2012).

[35] K. K. H. Shiba, T. Kawasaki, Apparent difference between 2d and 3d in supercooled liquids: Distinction between short-time vibrations and long-time configuration changes in dynamic heterogeneities, `arXiv:1510.02546` (2015).

[36] Z. Zheng, R. Ni, F. Wang, M. Dijkstra, Y. Wang, and Y. Han, Structural signatures of dynamic heterogeneities in monolayers of colloidal ellipsoids, *Nature communications*, **5** (2014).

[37] K. V. Edmond, M. T. Elsesser, G. L. Hunter, D. J. Pine, and E. R. Weeks, Decoupling of rotational and translational diffusion in supercooled colloidal fluids, *Proceedings of the National Academy of Sciences*, **109**, 17891–17896 (2012).

[38] L. Hong, S. M. Anthony, and S. Granick, Rotation in suspension of a rod-shaped colloid, *Langmuir*, **22**, 7128–7131 (2006).

[39] S.-H. Chong and W. Kob, Coupling and decoupling between translational and rotational dynamics in a supercooled molecular liquid, *Physical review letters*, **102**, 025702 (2009).

[40] J. Kim and B. J. Sung, Tracer shape and local media structure determine the trend of translation-rotation decoupling in two-dimensional colloids, *Phys. Rev. Lett.*, **115**, 158302 (2015).

[41] P. Debye, Polar molecules, new york, the chemical catalog co (1929).

[42] F. Fujara, B. Geil, H. Sillescu, and G. Fleischer, Translational and rotational diffusion in supercooled orthoterphenyl close to the glass transition, *Zeitschrift für Physik B Condensed Matter*, **88**, 195–204 (1992).

[43] I. Chang, F. Fujara, B. Geil, G. Heuberger, T. Mangel, and H. Sillescu, Translational and rotational molecular motion in supercooled liquids studied by nmr and forced rayleigh scattering, *Journal of non-crystalline solids*, **172**, 248–255 (1994).

[44] L. Berthier, D. Chandler, and J. P. Garrahan, Length scale for the onset of fickian diffusion in supercooled liquids, *EPL (Europhysics Letters)*, **69**, 320 (2004).

[45] S. K. Kumar, G. Szamel, and J. F. Douglas, Nature of the breakdown in the stokes-

einstein relationship in a hard sphere fluid, *The Journal of chemical physics*, **124**, 214501 (2006).

[46] M. K. Mapes, S. F. Swallen, K. L. Kearns, and M. Ediger, Isothermal desorption measurements of self-diffusion in supercooled o-terphenyl, *The Journal of chemical physics*, **124**, 054710 (2006).

[47] T. G. Lombardo, P. G. Debenedetti, and F. H. Stillinger, Computational probes of molecular motion in the lewis-wahnström model for ortho-terphenyl, *The Journal of chemical physics*, **125**, 174507 (2006).

[48] M. Kim, S. M. Anthony, S. C. Bae, and S. Granick, Colloidal rotation near the colloidal glass transition, *The Journal of chemical physics*, **135**, 054905 (2011).

[49] Y. Couder, J. M. Chomaz, and M. Rabaud, On the hydrodynamics of soap films, *Physica D*, **37**, 384–405 (1989).

[50] J. Plateau, *Statique expérimentale et théorique des liquides soumis aux seules forces moléculaires* (Gauthier-Villars, Paris) (1873).

[51] J. W. Gibbs, *The collected works* (Longmans Green, New York) (1931).

[52] V. Prasad and E. R. Weeks, Flow fields in soap films: Relating viscosity and film thickness, *Phys. Rev. E*, **80**, 026309–026309–7 (2009).

[53] V. Prasad and E. R. Weeks, Two-dimensional to three-dimensional transition in soap films demonstrated by microrheology, *Phys. Rev. Lett.*, **102**, 178302–178302–4 (2009).

[54] C. Cheung, Y. H. Hwang, X.-l. Wu, and H. J. Choi, Diffusion of particles in free-standing liquid films, *Phys. Rev. Lett.*, **76**, 2531–2534 (1996).

[55] J. Zhang, S. Childress, A. Libchaber, and M. Shelley, Flexible filaments in a flowing soap film as a model for one-dimensional flags in a two-dimensional wind, *Nature*, **408**, 835–839 (2000).

[56] M. A. Rutgers, Forced 2d turbulence: Experimental evidence of simultaneous inverse energy and forward enstrophy cascades, *Phys. Rev. Lett.*, **81**, 2244–2247 (1998).

[57] H. T. Tien and A. L. Ottova, The lipid bilayer concept and its experimental realization: From soap bubbles, kitchen sink, to bilayer lipid membranes, *Journal of Membrane Science*, **189**, 83–117 (2001).

[58] B. K. Martin, X. L. Wu, W. I. Goldburg, and M. A. Rutgers, Spectra of decaying turbulence in a soap film, *Phys. Rev. Lett.*, **80**, 3964–3967 (1998).

[59] J. M. Burgess, C. Bizon, W. D. McCormick, J. B. Swift, and H. L. Swinney, Instability of the Kolmogorov flow in a soap film, *Phys. Rev. E*, **60**, 715–721 (1999).

[60] A. A. Trapeznikov, Application of the method of two-dimensional viscosity and shear strength to the investigation of the structure and composition of two-sided films and surface layers in solutions of soaps and saponins, *Proceedings of the 2nd International Congress on Surface Activity*, pages 242–258 (1957).

[61] A. J. Levine and T. C. Lubensky, One- and two-particle microrheology, *Phys. Rev. Lett.*, **85**, 1774–1777 (2000).

[62] T. M. Fischer, P. Dhar, and P. Heinig, The viscous drag of spheres and filaments moving in membranes or monolayers, *J. Fluid Mech.*, **558**, 451–475 (2006).

[63] J. C. Crocker and D. G. Grier, Methods of digital video microscopy for colloidal studies, *J. Colloid Interface Sci.*, **179**, 298–310 (1996).

[64] A. V. Abraham, S. Ram, J. Chao, E. S. Ward, and R. J. Ober, Quantitative study of single molecule location estimation techniques, *Opt. Express*, **17**, 23352–23373 (2009).

[65] R. Parthasarathy, Rapid, accurate particle tracking by calculation of radial symmetry centers, *Nature Methods*, **9**, 724–726 (2012).

[66] C. L. Vestergaard, P. C. Blainey, and H. Flyvbjerg, Optimal estimation of diffusion coefficients from single-particle trajectories, *Phys. Rev. E*, **89**, 022726 (2014).

[67] R. Di Leonardo, F. Saglimbeni, and G. Ruocco, Very-long-range nature of capillary interactions in liquid films, *Phys. Rev. Lett.*, **100**, 106103 (2008).

[68] D. M. Kaz, R. McGorty, M. Mani, M. P. Brenner, and V. N. Manoharan, Physical ageing of the contact line on colloidal particles at liquid interfaces, *Nat. Mater.*, **11**, 138–142 (2012).

[69] X. L. Wu, R. Levine, M. Rutgers, H. Kellay, and W. I. Goldburg, Infrared technique for measuring thickness of a flowing soap film, *Rev. Sci. Inst.*, **72**, 2467–2471 (2001).

[70] J. Bechhoefer, J. C. Géminard, L. Bocquet, and P. Oswald, Experiments on tracer diffusion in thin free-standing liquid-crystal films, *Phys. Rev. Lett.*, **79**, 4922–4925 (1997).

[71] J. Sur and H. Kyu Pak, Capillary force on colloidal particles in a freely suspended liquid thin film, *Phys. Rev. Lett.*, **86**, 4326–4329 (2001).

[72] M. G. Nikolaides, A. R. Bausch, M. F. Hsu, A. D. Dinsmore, M. P. Brenner, C. Gay, and D. A. Weitz, Electric-field-induced capillary attraction between like-charged particles at liquid interfaces, *Nature*, **420**, 299–301 (2002).

[73] J. A. van Meel, D. Frenkel, and P. Charbonneau, Geometrical frustration: A study of four-dimensional hard spheres, *Phys. Rev. E*, **79**, 030201(R) (2009).

[74] P. Charbonneau, A. Ikeda, J. A. van Meel, and K. Miyazaki, Numerical and theoretical study of a monodisperse hard-sphere glass former, *Phys. Rev. E*, **81**, 040501(R) (2010).

[75] P. Charbonneau, A. Ikeda, G. Parisi, and F. Zamponi, Glass transition and random close packing above three dimensions, *Phys. Rev. Lett.*, **107**, 185702 (2011).

[76] D. J. Tritton, *Physical Fluid Dynamics (Oxford Science Publications)* (Oxford University Press, USA), 2 edition (1988), ISBN 0198544936.

[77] K. Zahn and G. Maret, Dynamic criteria for melting in two dimensions, *Phys. Rev. Lett.*, **85**, 3656–3659 (2000).

[78] A. T. Gray, E. Mould, C. P. Royall, and I. Williams, Structural characterisation of polycrystalline colloidal monolayers in the presence of aspherical impurities, *J. Phys.: Cond. Matter*, **27**, 194108 (2015).

[79] C. P. Kelleher, A. Wang, G. I. Guerrero-García, A. D. Hollingsworth, R. E. Guerra, B. J. Krishnatreya, D. G. Grier, V. N. Manoharan, and P. M. Chaikin, Charged hydrophobic colloids at an oil-aqueous phase interface, *Phys. Rev. E*, **92**, 062306 (2015).

[80] T. Narumi, S. V. Franklin, K. W. Desmond, M. Tokuyama, and E. R. Weeks, Spatial and temporal dynamical heterogeneities approaching the binary colloidal glass transition, *Soft Matter*, **7**, 1472–1482 (2011).

[81] L. D. Landau, Zur theorie der phasenumwandlungen II, *Phys. Zurn. Sowjetunion*, **11** (1937).

[82] N. D. Mermin, Crystalline order in two dimensions, *Phys. Rev.*, **176**, 250–254 (1968).

[83] B. Illing, S. Frischi, H. Kaiser, C. Klix, G. Maret, and P. Keim, Mermin-Wagner fluctuations in 2D amorphous solids, `arXiv:1510.05804v2` (2016).

[84] S. Mazoyer, F. Ebert, G. Maret, and P. Keim, Dynamics of particles and cages in an experimental 2d glass former, *Europhys. Lett.*, **88**, 66004 (2009).

[85] A. L. Thorneywork, R. Roth, D. G. A. L. Aarts, and R. P. A. Dullens, Communication: Radial distribution functions in a two-dimensional binary colloidal hard sphere system, *J. Chem. Phys.*, **140**, 161106 (2014).

[86] W. Kob and H. C. Andersen, Testing mode-coupling theory for a supercooled binary Lennard-Jones mixture: The van hove correlation function, *Phys. Rev. E*, **51**, 4626–4641 (1995).

[87] P. J. Steinhardt, D. R. Nelson, and M. Ronchetti, Bond-orientational order in liquids and glasses, *Phys. Rev. B*, **28**, 784–805 (1983).

[88] E. R. Weeks, J. C. Crocker, and D. A. Weitz, Short- and long-range correlated motion observed in colloidal glasses and liquids, *J. Phys.: Cond. Matter*, **19**, 205131 (2007).

[89] E. R. Weeks and D. A. Weitz, Properties of cage rearrangements observed near the colloidal glass transition, *Phys. Rev. Lett.*, **89**, 095704 (2002).

[90] S. Plimpton, Fast parallel algorithms for short-range molecular dynamics, *Journal of computational physics*, **117**, 1–19 (1995).

[91] E. Flenner and G. Szamel, Dynamic heterogeneity in two-dimensional supercooled liquids: comparison of bond-breaking and bond-orientational correlations, *arXiv preprint arXiv:1603.01343* (2016).

[92] A. Donev, F. H. Stillinger, and S. Torquato, Do binary hard disks exhibit an ideal glass transition?, *Phys. Rev. Lett.*, **96**, 225502 (2006).

[93] A. Donev, F. H. Stillinger, and S. Torquato, Configurational entropy of binary hard-disk glasses: Nonexistence of an ideal glass transition, *J. Chem. Phys.*, **127**, 124509 (2007).

[94] E. Rabani, J. D. Gezelter, and B. J. Berne, Calculating the hopping rate for self-diffusion on rough potential energy surfaces: Cage correlations, *J. Chem. Phys.*, **107**, 6867–6876 (1997).

[95] C. L. Klix, G. Maret, and P. Keim, Discontinuous shear modulus determines the glass transition temperature, *Physical Review X*, **5**, 041033 (2015).

[96] J. Fröhlich and C. Pfister, On the absence of spontaneous symmetry breaking and of crystalline ordering in two-dimensional systems, *Communications in Mathematical Physics*, **81**, 277–298 (1981).

[97] S. C. Kapfer and W. Krauth, Two-dimensional melting: From liquid-hexatic coexistence to continuous transitions, *Phys. Rev. Lett.*, **114**, 035702 (2015).

[98] H. Shiba, T. Kawasaki, and A. Onuki, Relationship between bond-breakage correlations and four-point correlations in heterogeneous glassy dynamics: Configuration changes and vibration modes, *Phys. Rev. E*, **86**, 041504 (2012).

[99] G. Williams, Time-correlation functions and molecular motion, *Chemical Society Reviews*, **7**, 89–131 (1978).

[100] S.-H. Chong, A. J. Moreno, F. Sciortino, and W. Kob, Evidence for the weak steric hindrance scenario in the supercooled-state reorientational dynamics, *Physical review letters*, **94**, 215701 (2005).

[101] G. L. Hunter, K. V. Edmond, M. T. Elsesser, and E. R. Weeks, Tracking rotational diffusion of colloidal clusters, *Optics express*, **19**, 17189–17202 (2011).

[102] M. Ediger and P. Harrowell, Perspective: Supercooled liquids and glasses, *The Journal of Chemical Physics*, **137**, 080901 (2012).

[103] Y. Jung, J. P. Garrahan, and D. Chandler, Excitation lines and the breakdown of stokes-einstein relations in supercooled liquids, *Physical Review E*, **69**, 061205 (2004).

[104] L. Berthier, Time and length scales in supercooled liquids, *Physical Review E*, **69**, 020201 (2004).

[105] L. J. Kaufman, Heterogeneity in single-molecule observables in the study of supercooled liquids, *Annual review of physical chemistry*, **64**, 177–200 (2013).

[106] K. Paeng and L. J. Kaufman, Single molecule rotational probing of supercooled liquids, *Chemical Society Reviews*, **43**, 977–989 (2014).

[107] K. Paeng, H. Park, D. T. Hoang, and L. J. Kaufman, Ideal probe single-molecule experiments reveal the intrinsic dynamic heterogeneity of a supercooled liquid, *Proceedings of the National Academy of Sciences*, **112**, 4952–4957 (2015).

[108] R. Zangi, S. A. Mackowiak, and L. J. Kaufman, Probe particles alter dynamic heterogeneities in simple supercooled systems, *The Journal of chemical physics*, **126**, 104501 (2007).

[109] S. A. Mackowiak, J. M. Noble, and L. J. Kaufman, Manifestations of probe presence on probe dynamics in supercooled liquids, *The Journal of chemical physics*, **135**, 214503 (2011).

[110] L. A. Deschenes and D. A. Vanden Bout, Heterogeneous dynamics and domains in supercooled o-terphenyl: A single molecule study, *The Journal of Physical Chemistry B*, **106**, 11438–11445 (2002).

[111] L. F. Cugliandolo, G. Gonnella, and A. Suma, Rotational and translational diffusion in an interacting active dumbbell system, *Physical Review E*, **91**, 062124 (2015).

[112] D. B. Hall, D. D. Deppe, K. E. Hamilton, A. Dhinojwala, and J. M. Torkelson, Probe translational and rotational diffusion in polymers near t g: roles of probe size, shape, and secondary bonding in deviations from debye–stokes–einstein scaling, *Journal of non-crystalline solids*, **235**, 48–56 (1998).

[113] M. G. Mazza, N. Giovambattista, H. E. Stanley, and F. W. Starr, Connection of translational and rotational dynamical heterogeneities with the breakdown of the stokes-einstein and stokes-einstein-debye relations in water, *Physical Review E*, **76**, 031203 (2007).